

Reconstructing accretion rates using OSL on a subsiding salt marsh

MSc Thesis

Sjoerd Postma

SGL-80436



3/26/2017

Wageningen UR

Postma, Sjoerd

Wageningen UR:

Prof. dr. J. Wallinga

Dr. T. Reimann

Alterra:

Ing. P.A. Slim

Dr. A.T. Kuiters

Reconstructing accretion rates using OSL on a subsiding salt marsh

MSc Thesis, 2017

Figure front page:

View from the sampling location at the Neerlands Reid, Ameland.

Photograph Nanny Heidema

S Postma

89 06 06 668 120

MSc Earth and Environment, specialisation Soil Geography and Landscape

Wageningen University

Supervisors:

Prof. dr. J. Wallinga
Dr. T. Reimann

Ing. P.A. Slim
Dr. A.T. Kuiters

Wageningen University

Wageningen Environmental Research (Alterra)

Abstract

To see whether it is possible to reconstruct accretion rates using high resolution OSL dating combined with Bayesian statistics, a subsiding salt marsh on the Dutch Wadden island Ameland was sampled. A secondary goal of the research was to investigate the marsh response on human-caused subsidence mimicking sea-level rise as predicted for the Dutch coast in the coming century. The accretion rate on the salt marsh had already been physically monitored for the last thirty years, but to see whether an acceleration of accretion rate had occurred, accretion rates from before that period had to be reconstructed.

It has been possible to date the profile at multiple depths and the reconstructed accretion rate is in agreement with the physically measured accretion rates on the upper part of the salt marsh. However, no indications of an increase in accretion rate were found, as the accretion rate seems to have been very stable for the last 50 years. In the period before 1960 there seems to have been a short period of higher accretion rates and before the 1940's a long period of lower accretion since the onset of salt marsh formation around 1890. It is not unlikely that factors such as the closing of the nearby Lauwerszee in 1969 have played a role in the accretion rates on the salt marsh and lack of a reaction to the subsidence in the deep subsoil.

Contents

Abstract	ii
List of Figures.....	v
List of Tables.....	vi
1. Introduction	1
1.1 Research objectives	2
2. Study area	3
3. Accretion on Salt Marshes.....	5
4. Methods.....	7
4.1 OSL-dating	7
4.1.1 Analysis protocols.....	7
4.1.2 Bleaching	8
4.2 ¹³⁷ Cs-dating	8
4.3 Sampling	9
4.4 Lab procedures.....	12
4.5 Performance testing	13
4.6 D _e determination	15
4.6.1 Sequence	15
4.6.2 Grain count	15
4.6.3 Analyst settings	15
4.7 Age Models	16
4.7.1 Iterative model	16
4.7.2 Central Age model.....	17
4.7.3 Minimum Age model	17
4.8 Dose Rate determination.....	18
4.8.1 Attenuation factors	19
4.8.2 Beta Dose rate	19
4.8.3 Gamma Dose Rate.....	21
4.9 OxCal model	21
5. Results	22
5.1 Results of the D _e measurements	22
5.2 Bleaching indicators	24
5.2.1 Skewness.....	24
5.2.2 Kurtosis	24
5.3 Iterative model outcomes	25
5.4 Bootstrap likelihood functions	26
5.5 Equivalent Doses according to different age models	28
5.6 Dose Rates	29
5.7 Ages for the different models.....	30
5.8 Choice of appropriate model	31
5.9 OxCal outputs	31

5.10 Final age determination.....	35
5.11 ¹³⁷ Cs dates.....	35
5.12 Accretion rates	37
6. Discussion.....	38
7. Conclusion	40
8. Recommendations	41
9. Acknowledgements.....	41
References.....	42
Appendix A: Sieving results	46
Appendix B: Porosity and Field capacity per texture class.....	47
Appendix C: Used formulas for calculations.....	48
Appendix D: Oxcal script.....	48
Appendix E: Map of the research area in 1854.....	49
Appendix F: Map of the research area in 1888.....	50
Appendix G: Map of the research area in 1897, created in 1910.....	51

List of Figures

Figure 1: Location of the study area, with the North Sea on the north side of the map, the Neerlands Reid, Kooioerdstuifdijk and Oerdsloot and the Wadden Sea in the south. With the white arrow indicating the sampled location.	1
Figure 2: Subsidence in cm beneath the research area between 1986 and 2011 (Ketelaar et al., 2011). In green the gas field ca. 3000 m below surface. Marker indicates research location.	2
Figure 3: Cross-section of the profile, with at 48 cm depth the year 1890 as expected age. Photograph Theo Jacobs.	3
Figure 4: Actual measured accretion rates on multiple locations on the salt marsh in mm/year for the period 1988-2014 (Krol, 2014). Arrow indicates sampling location along salt marsh creek Oerdsloot.	4
Figure 5: Model of the main factors influencing accretion on the salt marsh surface. Modification by French (2006) from USGS (1997).	5
Figure 6: Build up of the luminescent signal through time, with multiple bleaching events. From Preusser et al., 2008.	7
Figure 7: On the left; the equivalent dose samples in the profile. In the upper part of the profile thin 2.2 cm ø metal tubes were used, for the underlying package larger PVC tubes. On the right side 17 sampling tubes for ancient-DNA (another research).	9
Figure 8: Dose Rate samples NR-A to NR-F in the profile.	10
Figure 9: Tube NR-1a (2.2 cm ø, sampling depth 3.5 cm) opened with some roots and the sandy layers still clearly visible within the tube.	12
Figure 10: Results of the thermal transfer tests of NR-5 and NR-13.	13
Figure 11: Results of the dose recovery test.	14
Figure 12: Quartz decay curve of sample NR-2. First 0.48 s used as signal and the period from 0.48 to 1.76 s as early background (Cunningham and Wallinga, 2010).	15
Figure 13: Frequency distribution of a random sample (n=54) of the number of quartz grains on each aliquot. Average 24.5, standard deviation 9.7, minimum 10 and maximum 55.	15
Figure 14: Interpolated gamma radiation per layer (pers. com. N. Hobo).	21
Figure 15: Equivalent dose distributions of samples NR-1 to NR-8.	22
Figure 16: Equivalent dose distributions for sample NR-9 to NR-14.	23
Figure 17: Probability Density Functions of bootstrapped likelihoods of sample NR-1 to NR-8.	26
Figure 18: Probability Density Functions of bootstrapped likelihoods of sample NR-9 to NR-14.	27
Figure 19: Outcomes of different age models plotted versus depth. Iterative model, .Unlogged Central Age Model (CAMul) and unlogged 3-parameter Minimum Age Model (MAM3ul).	30
Figure 20: Table output of the bootstrapped likelihoods MAM3ul. All uncertainties are in 1-σ (68.2% certainty).	32
Figure 21: Table output of the Iterative model. All uncertainties are in 1-σ (68.2% certainty).	33
Figure 22: Age-depth model of the Iterative model. In red the salt marsh deposits and in green the underlying coastal plain deposits, separated by a boundary 'Boundary Change' with a top-hat-distribution at 51 cm depth. The position of 0 indicates the surface of the salt marsh at +1.51 NAP. For the sake of a better fit, a 'lower boundary' at 66 cm depth was added. Created using OxCal 4.3.1 (Bronk Ramsey, 2017).	34
Figure 23: ¹³⁷ Cs activity versus depth in cm below surface.	36
Figure 24: Accretion rate in cm/y through time	37
Figure 25: Porosity and Field capacity for multiple texture classes (from Dunne and Leopold, 1978).	47
Figure 26: Snip of the map of Ameland in 1854. White arrow indicating approximate sampling location. Original map from Tresoar: http://www.frieskaartenkabinet.nl/en/fries-kaartenkabinet/04992	49
Figure 27: Snip of the map of Ameland in 1888. White arrow indicating approximate sampling location. Original map from Tresoar: http://www.frieskaartenkabinet.nl/en/fries-kaartenkabinet/04321	50
Figure 28: Snip of the map of Ameland in 1897, produced in 1910. White arrow indicating approximate sampling location. Original map from Treasoar: http://www.frieskaartenkabinet.nl/en/fries-kaartenkabinet/04376	51

List of Tables

Table 1: The steps followed in the SAR protocol, as described in Murray and Wintle, (2000, 2003). The exact temperatures for the pre- and cut-heat were determined through a thermal transfer test.....	8
Table 2: Field form: Description of the profile at Neerlands Reid, (53°27'26.0"N 5°52'29.1"E), with texture class descriptions for the different depths, the depths of the sampling tubes and the type of tube used.	11
Table 3: Total tested aliquots and the amount of surviving aliquots for equivalent dose determination. .	16
Table 4: Number of surviving aliquots for different values of σ in the Iterative model	16
Table 5: Overdispersion of the samples	17
Table 6: σ_b sensitivity of the MAM3 _{ul}	17
Table 7: Measured water content, Loss on Ignition, un-attenuated beta Dose Rate (Gy/ka) and un-attenuated gamma Dose Rate (Gy/ka) of samples NR-A to NR-F and NR-11 to NR-14.	19
Table 8: Un-attenuated beta Dose Rate per sample, water content estimate per sample, LOI estimate per sample and attenuated beta Dose Rate per sample	20
Table 9: Bleaching indicators; overdispersion, skewness, kurtosis and difference between equivalent doses from the unlogged Central Age Model and unlogged 3-parameter Minimum Age Model.	24
Table 10: Number of tested aliquots per sample, luminescent aliquots per sample, number of accepted aliquots for the Iterative model and the averaged D_e -values.	25
Table 11: Equivalent Dose outcomes of the unlogged Central Age Model (CAM _{ul}), the Iterative model and the unlogged 3-parameter Minimum Age Model (MAM3 _{ul})	28
Table 12: Seperate Dose Rate contributions per sample (Gy/ka).	29
Table 13: Estimated Dose Rates (Gy/ka) for the different models.	29
Table 14: Outcomes of the unlogged Central Age Model (CAM _{ul}), the iterative model and the 3-parameter Minimum Age Model (MAM3 _{ul}).	30
Table 15: OxCal outcomes of the Iterative model, including re-added systematic errors for the samples	35
Table 16: Cs ¹³⁷ activity in Bq/g per sample.	35
Table 17: Determined accretion speeds in between sampling points and associated ages of the depths for which the accretion speed was determined.	37

1. Introduction

In the coming century, according to the Intergovernmental Panel on Climate Change (IPCC), a worldwide change in climate is expected to occur (IPCC, 2013). One of the effects of this climate change can be an acceleration of the relative sea level rise. In the Netherlands, relative sea levels have been rising since the onset of the Holocene and for the last centuries this relative sea level rise has been at a more or less constant rate (Guilcher, 1969, Ezer et al., 2015). An acceleration of this relative sea level rise will put more strain on coastal areas, especially natural areas that are outside of man-made coastal defences. Salt marshes are one of these type of areas, often forming an important natural addition to the coastal defences (King and Lester, 1995). Salt marshes also form an important ecological habitat, in which they are home to a diverse range of unique flora and fauna (Townend et al., 2011). It is however not clear how salt marshes will react to the expected acceleration in relative sea level rise and thus more knowledge is needed.

At Ameland, one of the west Frisian islands in the Wadden Sea a salt marsh developed behind a dike constructed in the period between roughly 1880-1890 (Figure 1). Underneath this salt marsh natural gas has been extracted since 1986, leading to a cup-shaped subsidence basin with a maximum subsidence of 35 cm in 2011 (Ketelaar et al., 2011) (Figure 2). As subsidence also leads to an increased relative sea level rise, this area can be indicative for the effects of accelerated relative sea level rise on salt marshes in the future. This becomes more clear when the rate of subsidence is compared to the predicted rate of relative sea level rise at the Dutch coast for the coming century. The Royal Dutch Meteorological Institute (KNMI, 2015) predicts a relative sea level rise of between 25 ('lowest'-scenario) and 80 cm ('highest'-scenario) between 2015 and 2085, which would equal rates between 0.35 cm/year for the 'lowest' and 1.14 cm/year for the 'highest'-scenario. These rates are comparable to the maximum subsidence rate experienced by the salt marsh at Ameland of 1.17 cm/year and a more general rate of 0.7 cm/year for the subsidence of 21 cm at the location sampled in this research.



Figure 1: Location of the study area, with the North Sea on the north side of the map, the Neerlands Reid, Kooioerstuifdijk and Oerdsloot and the Wadden Sea in the south. With the white arrow indicating the sampled location.

For any salt marsh to remain in place, it needs to accrete sediments at comparable rates to the relative sea level rise it experiences. Accretion on salt marshes is the result of a complex interaction of factors influencing rates in both positive and negative directions. The effect of a relative sea level rise on a natural system is that the sea can more easily enter the area during high tide and there is an increase in accommodation space (Townend et al., 2011). As a result accretion rate in the area will go up, as long as there is enough sediment available in the surrounding area and a means of transporting this sediment into the area (Townend et al., 2011). Under rising sea levels, salt marshes can undergo a couple of potential scenarios:

- The accretion keeps pace with the relative sea level rise and the salt marsh remains in place (Bartholdy et al., 2004).
- The inner part of a salt marsh lags behind and only the outermost, seaward, part keeps pace (Bartholdy et al., 2004).
- Transgression occurs, in which the salt marsh moves more inland towards higher ground or, when this is not possible, the salt marsh gradually drowns (Bartholdy et al., 2004, Kirwan et al., 2016).

1.1 Research objectives

The aims of this research were to accurately reconstruct the accretion rate for the last 130 years on the salt marsh at Ameland, using a combination of Optically Stimulated Luminescence (OSL) dating, ^{137}Cs -dating and Bayesian statistics. Multiple, stepwise, objectives were composed.

The first objective was to accurately date samples taken at different depths of the salt marsh using OSL dating. The second objective was to use this data to reconstruct historic accretion rates for the salt marsh, in order to have reference allowing comparison of accretion rates in more recent times. A third objective was

to see whether a change in accretion rate occurred in the last thirty years indicating a adaptation to an accelerated relative sea level rise as experienced by the salt marsh due to the subsidence in the deep subsoil.

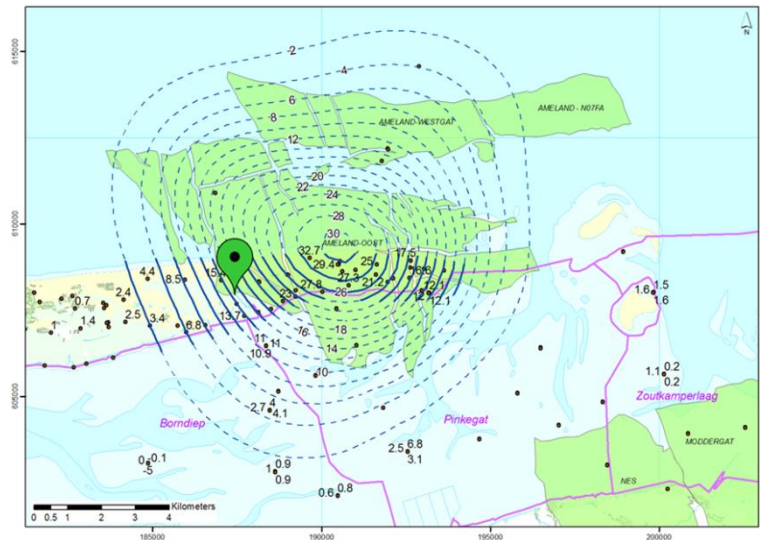


Figure 2: Subsidence in cm beneath the research area between 1986 and 2011 (Ketelaar et al., 2011). In green the gas field ca. 3000 m below surface. Marker indicates research location.

2. Study area

The salt marsh that was investigated in this research, called Neerlands Reid (Figure 1), developed on top of a coastal plain since approximately 1890, when on the north side of the area the Kooioerdstuifdijk was constructed to block the direct influence of the North Sea (Provinciaal Overlegorgaan Kust, 2000) (Figure 1). The location which was sampled is the levee of the largest tidal creek on the marsh. As the research location (53°27'26.0"N 5°52'29.1"E) is located in an outer bend, changes from an erosional to a depositional position are not expected and thus a continuous lithology is assumed.

This assumption is further supported by French and Stoddart (1992), who state that after an initial development phase, tidal networks on salt marshes tend to remain stable. Also salt marsh morphology seems to be close to equilibrium over time scales from decades to multiple centuries (Townend et al., 2011). A study of aerial photographs starting with pictures taken by the RAF during the second world war and a series of aerial photographs in 1959, 1969, 1979, 1986, 1990, 1992, 1996 and 2000 combined with a detailed map from 1931 (Appendix G) endorse these conclusions for the Neerlands Reid, as the creek has been in the same location for at least this period and most likely has been since the onset of the salt marsh formation. Tidal creeks such as the Oerdsloot tend to develop on the location of a pre-existing tidal channel (Redfield, 1972) and a map from the situation in 1854, before the closing of the Kooioerdstuifdijk, indicates the presence of a small tidal channel near the current location of the Oerdsloot (Appendix E).

The closing of the Kooioerdstuifdijk is thought to be seen in the subsoil as a sharp boundary around 50 cm depth between reduced silty clay loam layer on top of more sandy deposits (Figure 3). This sharp boundary is thought to stem from around 1890 and thus this will be used as a independent age control. The depth of this boundary varies with the location on the salt marsh, in the profile described by ISRIC it is found at 48 cm depth, where in this research it was found at 51 cm depth. There is a detailed description of the profile available by Stephan Mantel of ISRIC (2016). In the levee deposits, there is a fining-upward sequence of deposits on top of this clay layer, ranging from sandy loam in the lower part, to clay loam in the middle part. The top 10 centimetres consists of marine clay. Throughout the profile, there are sandy layers, varying in thickness from a few millimetres to a few centimetres. It seems likely that each of these sandy layers is the result of single storms or storm periods.

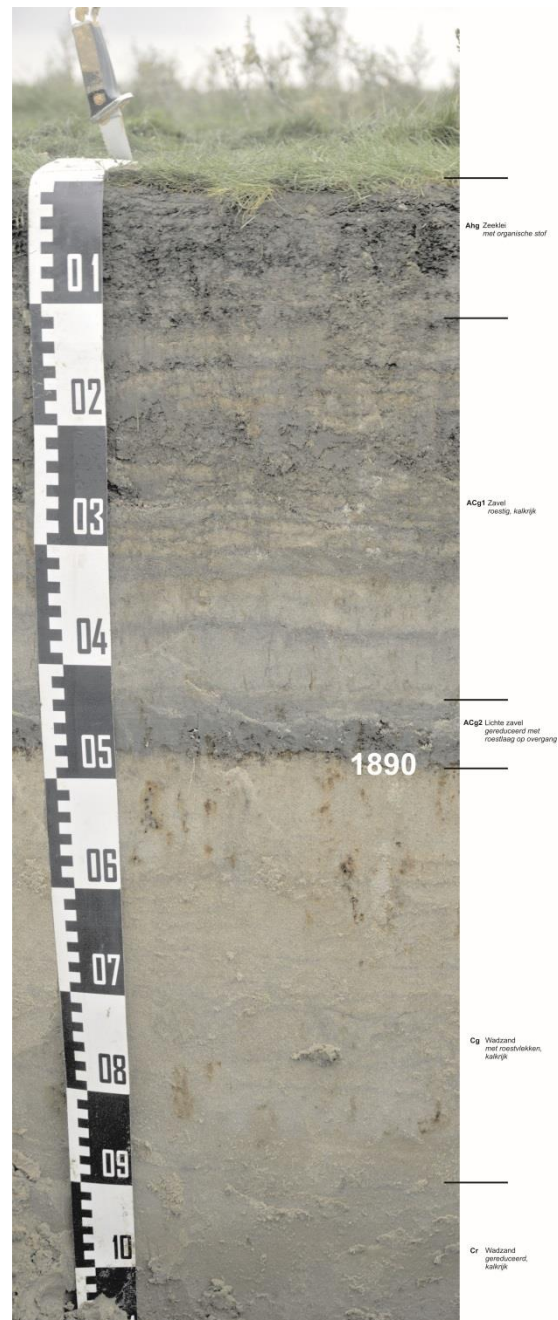


Figure 3: Cross-section of the profile, with at 48 cm depth the year 1890 as expected age. Photograph Theo Jacobs.

Part of the area is currently subsiding due to the mining of natural gas in the deep subsoil. As the area is part of a Natura2000 nature reserve, it has been closely monitored since the gas extraction started in the subsoil in 1986 (Figure 2, Ketelaar et al., 2011, waddenzee.nl). There are indications of regression in the area, such as the need for a small coast barrier along the Wadden edge to prevent abrasion by the sea. There is high resolution data on the development of different plant species in the area and since 1988 the accretion has also been physically monitored on six locations (Krol, 2014). On each of these locations a metal tile has been placed in the subsoil, on top of which each year the accretion is measured (Figure 4). These measurements show an accretion speed of in between 0.0, far away from the sea and 0.8 centimetres per year at the levee near the sea front (Figures 2 & 4; Krol, 2014). The sampled location is believed to have subsided by approximately 21 cm.



Figure 4: Actual measured accretion rates on multiple locations on the salt marsh in mm/year for the period 1988-2014 (Krol, 2014). Arrow indicates sampling location along salt marsh creek Oerdsloot.

3. Accretion on Salt Marshes

Most important factor in accretion on salt marshes is the sea as it is the main carrier of sediments for deposition. The Neerlands Reid salt marsh is likely to be mainly dependent on allochthonous (brought in from somewhere else) sediments (French, 2006), compared to marshes more dependent on autochthonous plant production, as it is in a meso-tidal environment (tidal range of between 2 and 4 meters, Uncles et al. (2002)). The hypothesis is that the subsidence due to gas extraction in the subsoil at our research location leads to a higher accessibility to the sea, through which the frequency of depositional events can increase leading to an enhanced accretion speed. However, as accretion on salt marshes is governed by a complex combination of multiple factors (Figure 5) such as setting, accommodation space, hydrodynamics, sediment supply, underlying morphology, sedimentation, salt marsh ecology and anthropogenic influences (Townend et al., 2011), this is not completely straightforward.

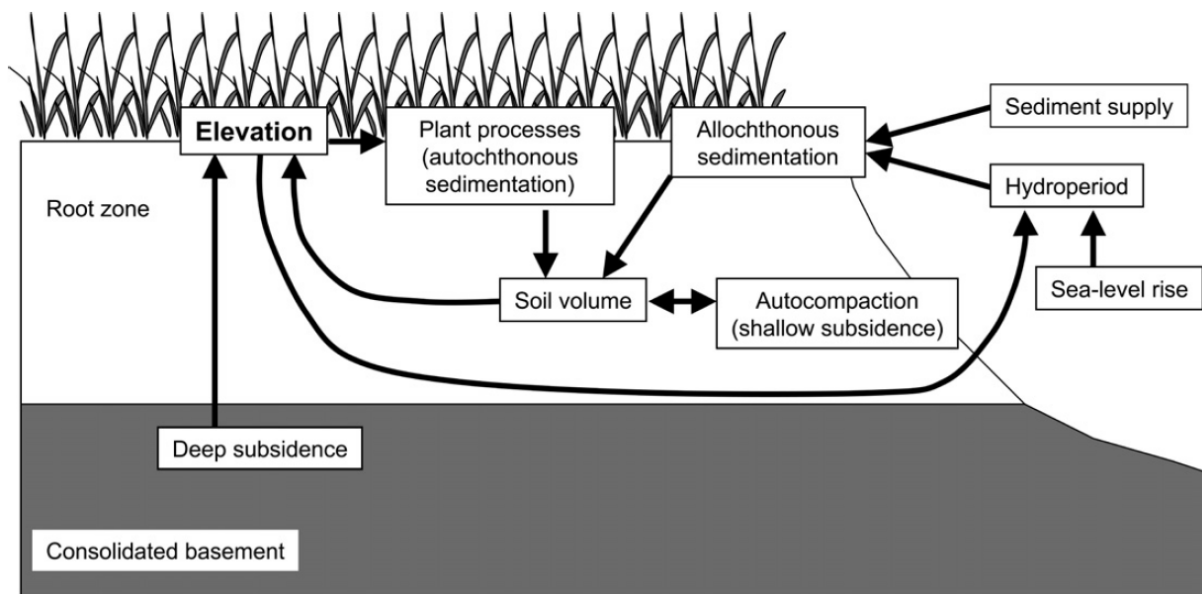


Figure 5: Model of the main factors influencing accretion on the salt marsh surface. Modification by French (2006) from USGS (1997).

Sediment supply is of great importance on accretion rates. Temmerman et al. (2004) modelled that for meso- and macro-tidal (more than 4 meter tidal difference (Uncles et al., 2002)) salt marshes in the Western Scheldt estuary a reduction of 50% in suspended sediment concentration (SSC) could lead to a predicted reduction of salt marsh elevation of 27 cm in 2100, where if the SSC was increased by a factor 2 the salt marsh elevation would increase by 25 to 31 cm for the same time period.

From research on macrotidal marshes accretion rates are thought to follow a parabolic trend, with high accretion speeds at the onset of marsh formation (Davidson-Arnott et al., 2002), which seems to be in agreement with Reed (1990), stating that the hydroperiod (the percentage of time that the marsh is submerged) is the most important factor determining sedimentation. Temmerman et al. (2004) state that salt marshes will quickly accumulate to a level around equilibrium with the local mean high-water level (MHWL), after which the accretion rates drop to a rate comparable to the MHWL rise.

Research by Schuerch et al. (2012) shows that both storm frequency as storm intensity have a large influence on accretion rates, with storm intensity becoming the largest factor after the salt marsh has reached a certain height. Storm intensity explains most of high accretion rates below a threshold value of 18 centimetres inundation, while storm frequency is the most important factor above this inundation depth. The existence of this threshold implies that accretion on higher salt marshes is mainly dependent on storm intensity, where lower salt marshes depend more on storm frequency. Vegetation seems to be the factor governing the threshold value. As the vegetation height on the salt marsh at Neerlands Reid has been restricted by grazing for most of its existence, it is not unlikely that this threshold value is lower here and storm frequency is of more importance than for a more typical un-grazed salt marsh.

Another important factor governing depositional sequences on salt marshes is autocompaction, which is the reduction of sediment volume after deposition. This autocompaction of sediments is made up out of two separate processes (Audet, 1995); consolidation through the loss of pore fluid under increased load and compression through the increasing overburden of overlying sediments. The more allochthonous the salt marsh is, the less effect this autocompaction will have, as clastic sediments are less prone to the mentioned processes than peat from plant production is (French, 2006). From the same paper comes that autocompaction is mainly of importance around the middle of the sedimentary history, when underlying older sediments are being compacted by continuing sedimentation. At later stages, when accretion is close to the MHWL rise, the effects of autocompaction become negligible.

On a back barrier salt marsh Skallingen, Denmark, 63% of the yearly deposition can be explained by the North Atlantic Oscillation (NAO) winter index, as it is the forcing factor for magnitude and number of overmarsh tides (Bartholdy et al., 2004). This index describes the deviation from the average difference between the sea level pressure in Portugal (Lisbon) and in Iceland (Stykkisholmur) (Lamb and Pepler, 1987). There is also evidence suggesting that salt marsh accretion rates are related to the lunar cycle of 18.6 years, with enhanced biological growth and reduced mineralogical sedimentation during phases of increased tidal range and vice versa (French, 2006).

4. Methods

4.1 OSL-dating

In this research, the accretion speed was determined using Optically Stimulated Luminescence (OSL) dating. OSL is a dating method for sediments first described by Huntley (1985), whereby the time passed since the burial of a quartz or feldspar grain can be measured. In this research we have focused on quartz OSL. The method is based on the excitement of electrons through natural ionising radiation. When excited, these electrons will move from their normal state in the valence band, to a higher energy state in the conduction band. Some of these electrons are trapped when moving back to a lower energy level in a so-called electron trap, this causes them to remain in a higher energy state. Some of these traps are stable and thus fill up with electrons through time.

Exposure to light and/or heat can empty these traps (Figure 6), after which the electrons fall back into their original, low-energy state. When electrons fall back into their low energy state they sometimes emit a measurable light pulse. The intensity of this light pulse is measured and indicates the amount of radiation received since the signal was last reset; this is known as the equivalent dose (D_e). When the amount of radiation the sample received per time unit, the Dose Rate (DR), is known then the time since the last exposure to (day)light can be determined by dividing the D_e through the DR like:

$$Age (year) = \frac{\text{equivalent dose (Gy)}}{\text{dose rate } (\frac{Gy}{y})}$$

As the samples can only have been exposed to sunlight during and shortly after deposition, this is then the time that has passed since deposition and subsequent burial.

4.1.1 Analysis protocols

For a correct determination of D_e -values there are a couple of conditions that need to be fulfilled. Following Murray and Wintle (2000, 2003);

- Competition for trap filling is the same for laboratory and natural irradiation.
- The electron traps are stable for the relevant period.
- All traps are completely emptied (bleached) during deposition.
- The OSL response (so the amount of photons which are released for each unit of trapped charge) is the same for the measurement of the natural signal as for the laboratory induced signals.

To eliminate this last condition, the single-aliquot regenerative-dose (SAR) protocol was developed by Murray and Wintle (2000, 2003). In this protocol, the aliquots are tested for any changes in luminescence sensitivity that might occur during the recharging of the aliquots. For this research, this SAR protocol was used.

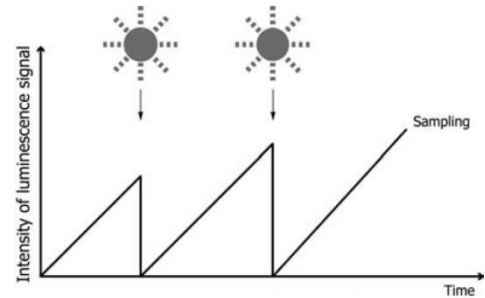


Figure 6: Build up of the luminescent signal through time, with multiple bleaching events. From Preusser et al., 2008

SAR protocol

The SAR protocol consists of a series of repeated measuring cycles on each of the separate aliquots (Table 1). The used temperatures and doses were determined in a thermal transfer test. In the first cycle of the SAR, the natural signal is read out. The luminescent sensitivity is determined by dividing the natural dose L_n through the test dose T_n . In the following cycles any changes in luminescent sensitivity due to the

recharging of luminescent signal are measured and corrected for by comparing the T_x/T_n -ratio for each of the SAR-cycles. The following acceptance criteria were used in the analysis of the samples; recycling ratio limit; 20%, max test dose error; 20%, max recovery as percentage of the largest R; 10%.

Table 1: The steps followed in the SAR protocol, as described in Murray and Wintle, (2000, 2003). The exact temperatures for the pre- and cut-heat were determined through a thermal transfer test.

Step	Treatment	Observed
1	Give dose (or natural for first cycle)	-
2	Preheat (180 °C for 10 seconds)	-
3	Stimulate for 20 s at 125 °C	L_i
4	Give test dose, D_t	-
5	Heat to 160 °C	-
6	Stimulate for 20 s at 125 °C	T_i
7	Hot bleach at 190 °C	-
8	Return to 1	

4.1.2 Bleaching

Poor bleaching is the incomplete resetting of the OSL-signal at deposition. This can lead to (large) overestimates of ages because the latent luminescence signal is also included in the measurement of D_e -values. There are multiple indicators that can be used to determine poor bleaching. The skewness and kurtosis of the D_e -distribution can tell something about the degree of bleaching (Bailey and Arnold, 2006), and so does the overdispersion of the data (Olley et al., 2004). Wallinga (2002a) advises to use small aliquots to increase the chances of detecting poor bleaching and take both the spread of the D_e -values as well as the symmetry of the dose distributions into account. It is impossible to be completely sure that there is no poor bleaching in a sample, but a tight, symmetrical dose distribution is a good indicator (Wallinga, 2002b). Cunningham et al. (2015) defined a 'poor bleaching'-score based on the D_e -distribution. This can then be used as a way of comparing bleaching between samples. Finally the difference between the modelled outcomes of the CAM_{ul} and the $MAM-3_{ul}$ can tell something about the spread within the distribution. In a perfectly bleached sample this difference will be small, where in a poorly bleached sample this difference is large again due to the spread in the data. When poor bleaching is found, this can be an indication of limited light exposure prior to sedimentation.

4.2 ^{137}Cs -dating

As ^{137}Cs is one of the radionuclides which is measured in the DR-samples for OSL-dating, it is used as a rough independent age control in this research. ^{137}Cs is an anthropogenic radionuclide which, in case of the North Sea area, came in the environment in three main events. The first peak in ^{137}Cs concentration would be from the late 1940's to the zenith of above-ground nuclear weapon testing in 1963, also known as the 'bomb-spike' (Walhgren and Nelson, 1972). A second peak would be caused by wastewater from the Sellafield nuclear complex around 1980 (Madsen et al., 2005) and the last from the Chernobyl nuclear disaster in 1986 (Walker, 2005). In similar salt marshes in Denmark, the Chernobyl peak is most distinct (Madsen et al., 2005), but it can also be that the two peaks blend into a broader peak due to the dynamic nature of the area in which sediments are reworked. In another (younger) salt marsh on Ameland (De Hon) and salt marshes on the mainland coast opposite Ameland the Chernobyl peak is detected (pers. comm. A.V. de Groot).

4.3 Sampling

As the profile has a form of layering of different texture classes and OSL dating is based on quartz, small diameter tubes were used to sample the more sandy layers to insure there was enough quartz for measuring and come to a high resolution depth model. For the upper part of the profile, where a higher precision was needed, thin 2.2 cm \varnothing metal tubes were hammered into the wall. For the lower parts, thicker PVC tubes were used (Figure 7).

To be sure enough material was yielded, the metal tubes were used in sets of three (a, b and c from left to right) and filled with a small piece of Styrofoam to help the sediment stay in place during hammering (Figure 7). For the lower lying, more massive homogenous complexes, thicker, 4.5 cm \varnothing PVC tubes were used. Here, the DR was measured using the outer, potentially bleached during sampling, parts of the tubes.

After being hammered into the wall, the still exposed sides were covered in order to keep the contents of the tubes in place and cover them from any incoming light. For the metal tubes rubber floor protectors were used as cover, for the larger diameter PVC tubes black gaffa tape was used and for the largest tube (NR-14) a plastic lid was available.



Figure 7: On the left; the equivalent dose samples in the profile. In the upper part of the profile thin 2.2 cm \varnothing metal tubes were used, for the underlying package larger PVC tubes. On the right side 17 sampling tubes for ancient-DNA (another research).

Next to the small diameter metal D_e tubes, separate samples for DR determination were taken (Figure 8). As part of the DR is build up by gamma radiation, which has an attenuation of approximately 30 cm in soils and these sandy layers tend to have a lower radioactivity then the more clayey surrounding layers a DR determination of the smaller tubes would lead to an underestimation of the DR-values.

Sampling took place a couple of hours after the tidal cycle was at its lowest point and the last rainfall event (5 mm, measured at the NAM gas-extraction site 3.2 km away) was three days before the sampling, followed by two dry and hot days. The top of the profile was at a height of +1.51 meters above the Amsterdam Ordnance Datum (NAP) and tides in the month before sampling had not been above +1.39 m NAP, so the profile was in a relatively dry state.

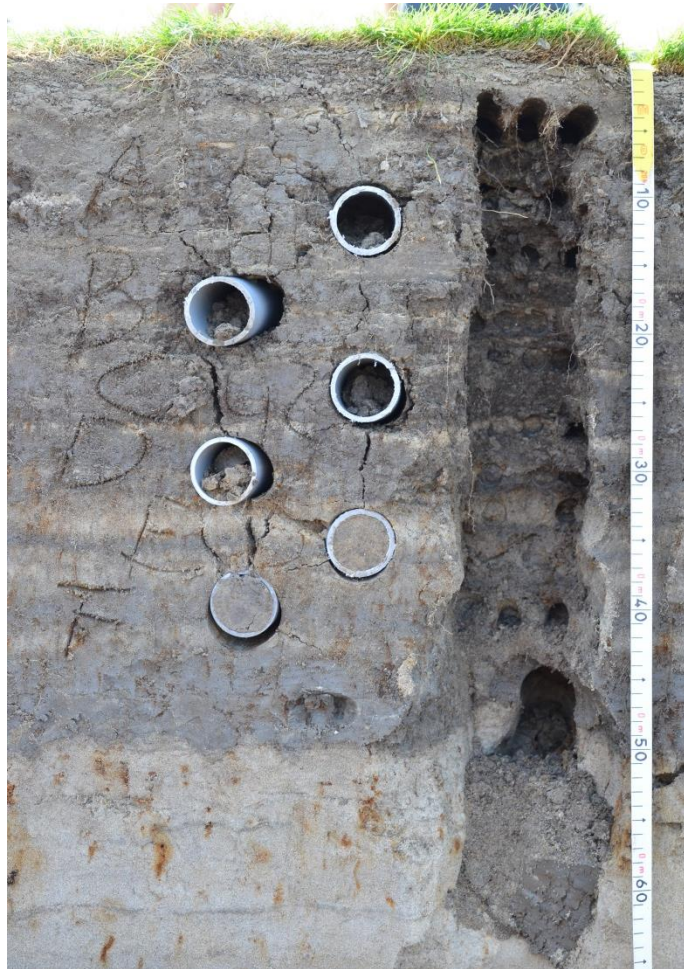


Figure 8: Dose Rate samples NR-A to NR-F in the profile

Table 2: Field form: Description of the profile at Neerlands Reid, (53°27'26.0"N 5°52'29.1"E), with texture class descriptions for the different depths, the depths of the sampling tubes and the type of tube used.

Field-code (NR-#)	Depth (cm, centre of tube)	NAP (m)	Type of tube	Description, remarks
1	3.5	+1.475	Three, thin, 15 cm long, 2.2 cm ø metal tubes	Sandy layer, 1 cm of clean sand surrounded by (clay-)loamy material, many roots
2	9.0	+1.42	Three, thin, 15 cm long, 2.2 cm ø metal tubes	Centre of rather homogenous, 8 cm thick loamy formation
3	14.0	+1.37	Three, thin, 15 cm long, 2.2 cm ø metal tubes	Unclear sandy layer with loamy sand, within a 2 cm thick loam-sand alternation
4	19.0	+1.32	Three, thin, 15 cm long, 2.2 cm ø metal tubes	Unclear sandy layer, 0.5-1 cm thickness
5	22.5	+1.285	Three, thin, 15 cm long, 2.2 cm ø metal tubes	More sandy layer, within 3 cm thick sand/loam alternation. Underneath there is a 4 cm clay loam layer (24-28 centimetre depth)
6	28.5	+1.225	Three, thin, 15 cm long, 2.2 cm ø metal tubes	Relative clean sandy layer, 1-1.5 cm thickness
	29-31.5			Clay loam
7	32.5	+1.185	Three, thin, 15 cm long, 2.2 cm ø metal tubes	Unclear sandy layer laminated with clay loam bands
8	35.5	+1.155	Three, thin, 15 cm long, 2.2 cm ø metal tubes	Relative clean sand, 3 cm thickness; Underneath there is a 1 cm loamy/clay loamy layer, underneath that more sand
9	39.0	+1.12	Three, thin, 15 cm long, 2.2 cm ø metal tubes	4 cm of sand, unclear transitions. Underneath there is a more loamy layer of 3 centimetre thickness
10	44.0	+1.07	Three, thin, 15 cm long, 2.2 cm ø metal tubes	Lowest lying sand layer from a sandy formation of 3 cm thickness
	45-50			Clay loam
11(b)	48.5	+1.025	25 cm long, 4.5 cm ø PVC tube	Large diameter tube in Clay loam, later moved 30 cm to the side because the first tube crossed the boundary with the underlying package deeper in the wall.
	51.0	+1.00		Sharp boundary with underlying homogenous sand. Sharp boundary, but varying by 3 cm in depth
12	54.5	+0.965	25 cm long, 4.5 cm ø PVC tube	Large diameter tube, just below boundary in homogenous sand formation
13	63.0	+0.88	25 cm long, 5 cm ø PVC tube	Large diameter tube in homogenous sand
14	79.0	+0.72	20 cm long, 7.5 cm ø PVC tube	Large diameter tube in homogenous sand
A	11.5	+1.395	25 cm long, 4.5 cm ø PVC tube	Large diameter tube for Dose rate determination
B	19.0	+1.32	25 cm long, 4.5 cm ø PVC tube	Large diameter tube for Dose rate determination
C	24.5	+1.265	25 cm long, 4.5 cm ø PVC tube	Large diameter tube for Dose rate determination
D	31.0	+1.20	25 cm long, 4.5 cm ø PVC tube	Large diameter tube for Dose rate determination
E	36.0	+1.15	25 cm long, 4.5 cm ø PVC tube	Large diameter tube for Dose rate determination
F	41.0	+1.10	25 cm long, 4.5 cm ø PVC tube	Large diameter tube for Dose rate determination
Other remarks				Ants (<i>Lasius</i>) in the surrounding area down to 20 cm Roots down to 30 cm observed Gley spots down to 75 cm depth

4.4 Lab procedures

After sampling in the field, the samples were taken to the Netherland Centre for Luminescence dating NCL in Wageningen (<http://www.wur.nl/en/Expertise-Services/Research-Institutes/Environmental-Research/Facilities-Products/Laboratories-Environmental-Sciences-Group/NCL-Netherlands-Centre-for-Luminescence-dating.htm>) to be opened under subdued orange light, in order to prevent loss of signal before measuring.

First, the outer parts of the metal sampling tubes (NR 1-10) were removed, using a simple tube cutter and a bench vice to secure the tube (Figure 9). These had to be cut open, as otherwise due to the small diameter there was too much risk of contaminating the D_e material on the inside with potentially bleached material from the outer sides when removing it from the tube.

On the side which had been hammered into the wall, at least the outer centimetre was removed. For the outer facing side this depended on the amount of filling of the tube. At least 3 centimetre of filled tube was cut off. Often, this meant removing 5 centimetres of tube, 3 centimetre of material filled tube and 2 centimetre of 'empty' space, mainly filled with Styrofoam from the sampling procedure.

For the thicker tubes a similar procedure was carried out in which the outer 4 centimetres from both sides were removed using a scalpel.

Afterwards, the D_e material of NR 1-10 was wet sieved for fractions <180, 180-212, 212-250 and >250 μm . The most left (sample NR-1a, NR-2a etc.) of the in triplo sampled tubes were used, as these were located nearest to the DR samples, resulting in the best possible DR estimate for the samples. Before sieving the material from the tubes it was however unclear whether these tubes alone would yield enough quartz for a proper D_e determination. After sieving, the 180-212 fraction was taken as this had the most material. With this information in mind, the larger volume samples were only sieved for <180, 180-212 and >212 μm .

After sieving all of the samples, the chosen fraction was treated as described in Wintle (1997). First with 10% HCl for 40 minutes to remove any calcium carbonates and after that with 10% H_2O_2 to remove organic matter. For the H_2O_2 procedure, the samples were placed in the 10% solution for as long as any reaction occurred, in practice this meant leaving the samples over the weekend. Following this, the samples were etched for 5 minutes with 10% HF and 40 minutes with 40% HF. This dissolves feldspars, which is, alike quartz, a luminescent mineral. It also serves to etch away the outer 10 μm of the quartz, which is potentially effected by alpha radiation. To remove any fluorides that may have formed during the previous step, the samples were treated again for 60 minutes with 10% HCl. As an IR test showed no feldspar contamination of the samples, the additional step of using a density separation to remove any remaining feldspars from the samples was skipped.



Figure 9: Tube NR-1a (2.2 cm ϕ , sampling depth 3.5 cm) opened with some roots and the sandy layers still clearly visible within the tube.

4.5 Performance testing

As the luminescent characteristics of quartz can vary different regions of the world, a couple of tests had to be done before measuring of D_e -values could commence. This is also for testing the best way of determining the D_e -values. Both a dose recovery (Murray and Wintle, 2003) as a thermal transfer test (Murray and Wintle, 2000) were done to check whether the chosen protocols functioned properly.

Thermal transfer

In order to find the correct pre- and cut-heat for the measurement protocol, sample NR-5 and NR-13 were completely bleached and subsequently heated up to temperatures varying from 180 to 280 °C. This is to see at what temperature charge from more stable (harder to stimulate) traps would transfer to the 125 °C trap that is normally measured in this research. See Figure 10 below for the results. Based on these outcomes the choice was made to use a 10 s preheat and cut heat of 180 °C.

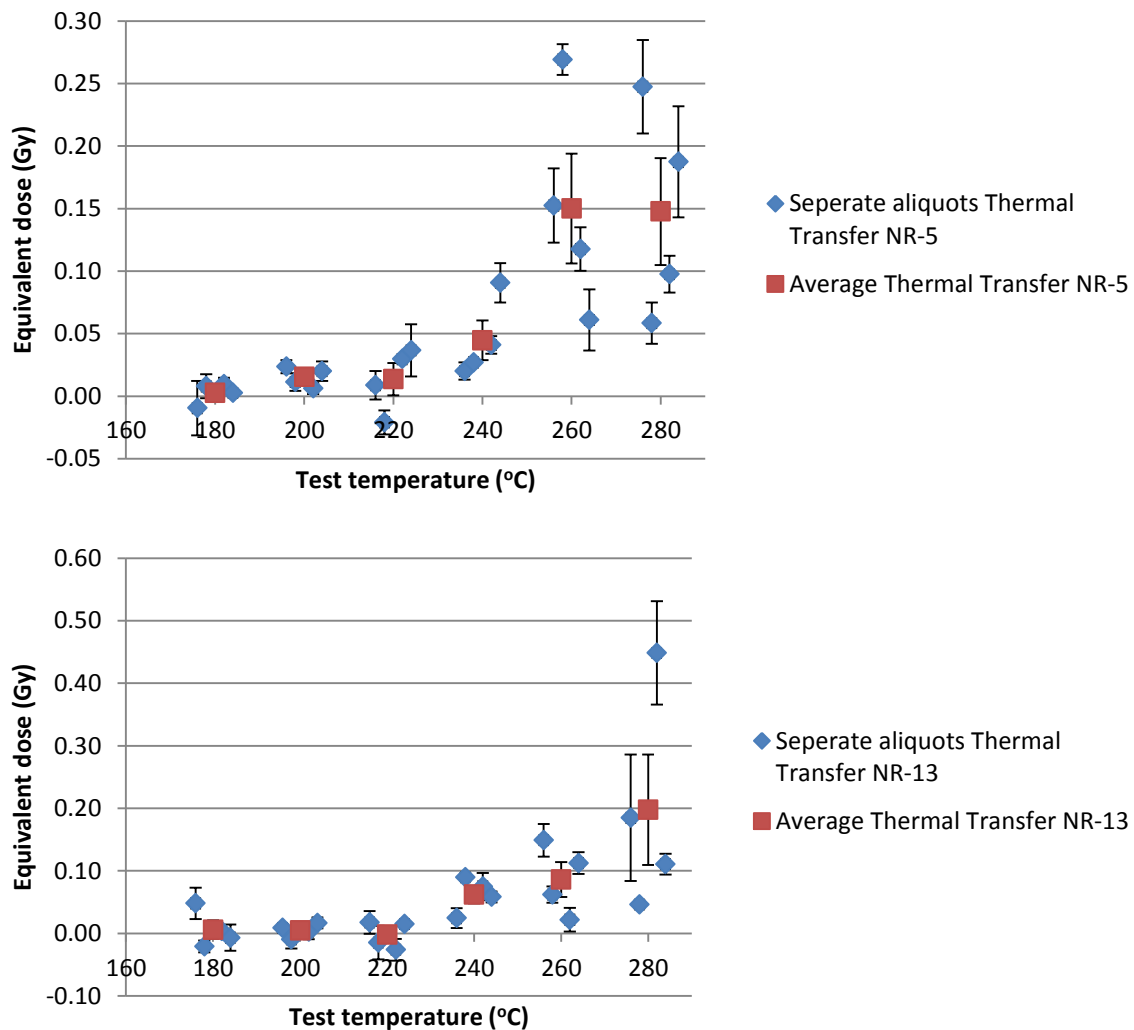


Figure 10: Results of the thermal transfer tests of NR-5 and NR-13.

Dose recovery

A dose recovery test (Figure 11) was done to check the luminescent properties of the quartz as well as the survival rate of the acceptable errors in the measurement. Since we wanted to measure on single grain scale, 1 mm discs were used and the goal was to achieve a survival rate of 50%.

In this test, the luminescent traps of the samples are fully emptied (bleached) by exposing them (twice) to blue LED light for 300 seconds at 20 °C. After bleaching, the samples are given a known dose of 2.613 Gray (Gy), in which one Gray stands for the absorption of one joule of ionizing radiation per kilogram of matter. Afterwards, the SAR protocol as described in Murray and Wintle (2000, 2003) and reviewed in Wintle and Murray (2006) was used. The 10 second pre-heat of 180 °C and a cut-heat of 180 °C as found in the Thermal Transfer test were used. For the signal the early-background approach as described by Cunningham and Wallinga (2010) was used, in which the integral 26 to 88 are used to determine the background and afterward subtracted from the first 25 integrals to find the OSL-signal. Error margins were set at 20% to insure a proper survival rate was achieved.

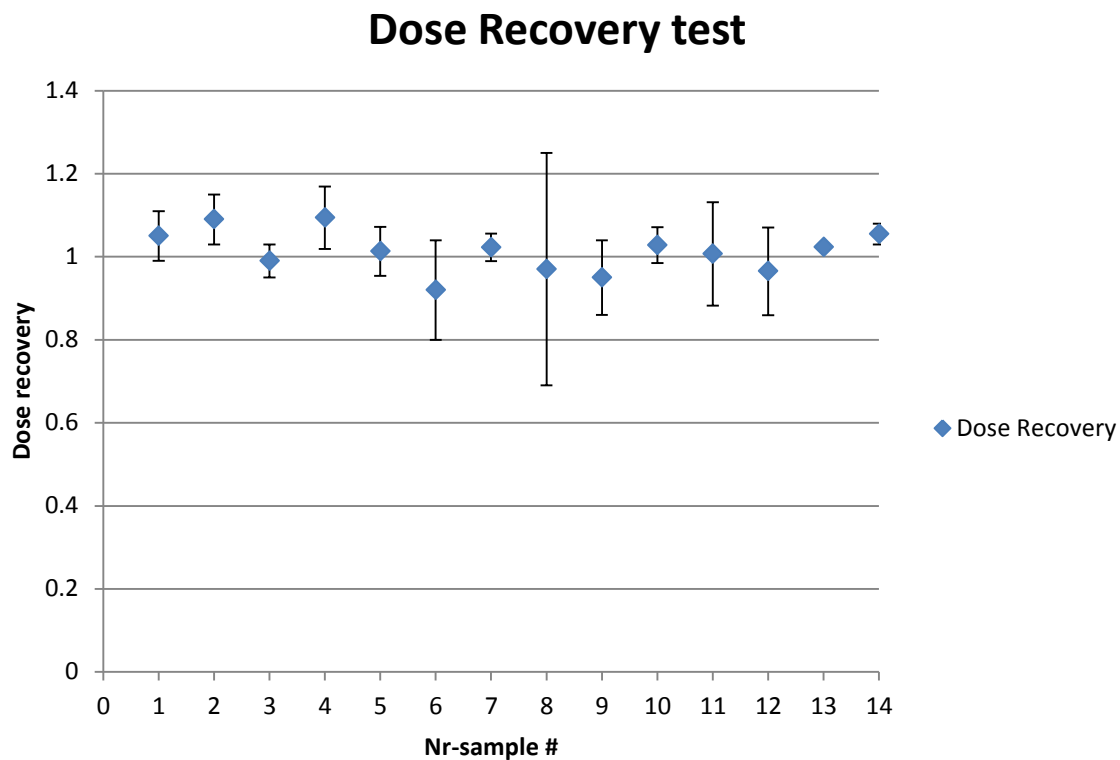


Figure 11: Results of the dose recovery test

4.6 D_e determination

4.6.1 Sequence

All discs measured for equivalent dose determination were checked for feldspar contamination through a IR-wash (Duller, 2003) since low energy photons from the infrared (IR) band will stimulate luminescence in feldspars, but not in quartz (Hütt & Jaek, 1989). For equivalent dose determination, the Single Aliquot Regeneration (SAR) protocol, as described by (Murray and Wintle, 2000) and reviewed in Wintle and Murray (2006), was used. This protocol is designed to compensate for any sensitivity changes that can occur during the measurement cycle. In the procedure the aliquot is measured repeatedly, the first time to measure its natural OSL signal and afterwards to measure its response to a known given test dose, in our case 4.3 Gy, equalling a 50 second exposure to a 0.869 Gy/s

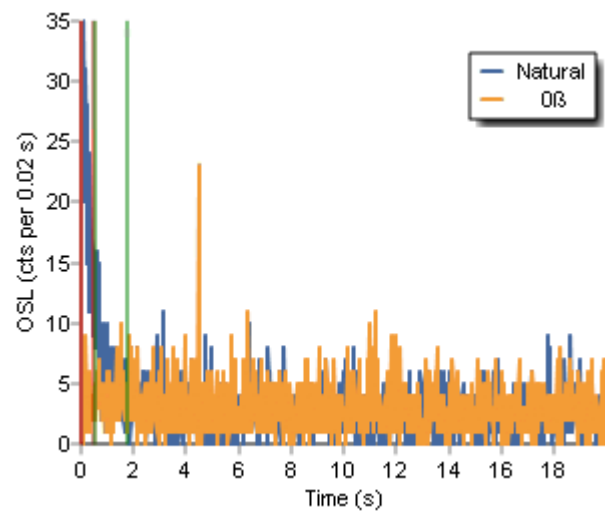


Figure 12: Quartz decay curve of sample NR-2. First 0.48 s used as signal and the period from 0.48 to 1.76 s as early background (Cunningham and Wallinga, 2010).

beta source. As this is done repeatedly with the same dose, any change in sensitivity is measured and can be corrected for. For the analysis of the then found data, the early background approach of Cunningham and Wallinga (2010) was used. In this research, the background value which is subtracted from the signal was the averaged value from channel 26-88 (in which every channel stands for 2 ms), multiplied by the amount of channels used (Figure 12).

4.6.2 Grain count

The goal was to measure on a single (luminescent) grain scale, as this is preventing the averaging of multiple grains and thus keeping the spread between separate grains intact.

Due to limited availability of the lab and for convenience sake, a proxy of around 30 quartz grains per aliquot was used, as approximately only 1-5% of quartz grains show luminescent characteristics. To achieve this a 1 mm mask was used. The true amount of grains on the aliquots was monitored by randomly picking two discs from each set of 16 measured aliquots and counting the amount of grains under a microscope. In total, 54 aliquots were analysed, which lead to an average amount of 24.5 grains per aliquot, with a minimum of 10, a maximum of 55 and a standard deviation of 9.7 (Figure 13).

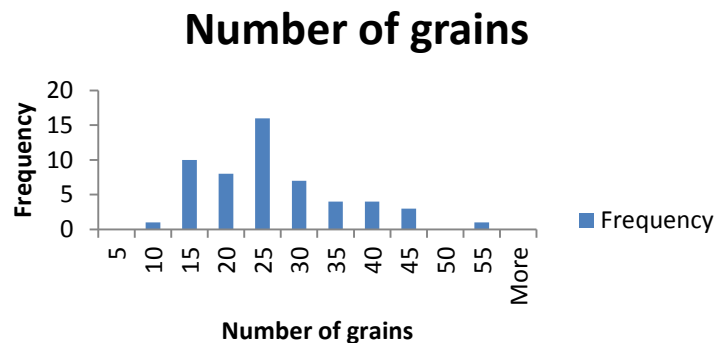


Figure 13: Frequency distribution of a random sample (n=54) of the number of quartz grains on each aliquot. Average 24.5, standard deviation 9.7, minimum 10 and maximum 55.

4.6.3 Analyst settings

The standard RisøTL/OSL software package 'Analyst' was used. The aim was to have a aliquot survival ratio of around 50%. To achieve this, a measurement error of 0.5% was allowed, data was calculated using 1000 Monte Carlo repeats, the recycling ratio limit was set at 10% and both the maximum test dose error as the max recovery as a percentage of the largest R were set at 20%.

A number of 20 accepted aliquots for each of the samples was taken as a minimum before using the results of the measurement as input for the different age models. In an attempt to reduce the scatter and lower the equivalent dose errors from samples NR-3, NR-5 and NR-10 even more aliquots were measured (Table 3).

Table 3: Total tested aliquots and the amount of surviving aliquots for equivalent dose determination.

NR-#	Total tested aliquots	Number of luminescent aliquots	Percentage surviving aliquots
1	64	24	37.5%
2	48	22	45.8%
3	96	37	38.5%
4	48	26	54.2%
5	96	45	46.9%
6	64	25	39.1%
7	48	22	45.8%
8	48	27	56.3%
9	48	25	52.1%
10	96	42	43.8%
11	48	26	54.2%
12	48	30	62.5%
13	48	28	58.3%
14	64	26	40.6%
Sum	864	405	Average: 48.3%

4.7 Age Models

The found equivalent doses were analysed using three different models, in order to come to the best analysis of the data.

4.7.1 Iterative model

This very simple model rejects any aliquot which lies outside a given σ standard deviation of the sample population. After removing these aliquots from the population, this process is done 5 times in an iterative process. The then remaining aliquots are then used for age determination. After trying multiple values of σ (Table 4), the choice was made to use a σ of 1.5, as this removed the large, more extreme outliers but kept the general spread within the data intact and the amount of accepted aliquots above 50%.

Table 4: Number of surviving aliquots for different values of σ in the Iterative model

NR-#	Number of aliquots	Iterative model; 1- σ		Iterative model; 1.5- σ		Iterative model; 2- σ	
		Number of accepted aliquots		Number of accepted aliquots		Number of accepted aliquots	
1	24	6	25.0%	14	58.3%	20	83.3%
2	22	8	36.4%	13	59.1%	17	77.3%
3	37	9	24.3%	22	59.5%	30	81.1%
4	26	7	26.9%	16	61.5%	19	73.1%
5	45	16	35.6%	28	62.2%	35	77.8%
6	25	8	32.0%	12	48.0%	19	76.0%
7	22	6	27.3%	13	59.1%	16	72.7%
8	27	6	22.2%	14	51.9%	20	74.1%
9	25	4	16.0%	15	60.0%	20	80.0%
10	42	8	19.0%	23	54.8%	33	78.6%
11	26	5	19.2%	13	50.0%	19	73.1%
12	30	6	20.0%	18	60.0%	21	70.0%
13	28	6	21.4%	16	57.1%	22	78.6%
14	26	5	19.2%	15	57.7%	21	80.8%

4.7.2 Central Age model

The unlogged version of the Central Age Model (CAM_{ul}) (Galbraith et al., 1999, Arnold et al., 2009) was used to determine the overdispersion within the equivalent dose data and to offer a comparison to the unlogged 3-parameter Minimum Age Model and the Iterative model, as small differences between the Minimum Age Model and the Central Age Model indicate a Gaussian or near-Gaussian distribution of the equivalent dose data. These outcomes can then be used as indication of the completeness of the OSL signal resetting at deposition, this is known as bleaching.

Table 5: Overdispersion of the samples

NR-#	Overdispersion
1	56.6%
2	63.8%
3	56.4%
4	37.7%
5	70.1%
6	26.3%
7	1.1%
8	21.2%
9	12.5%
10	60.0%
11	22.8%
12	21.9%
13	10.7%
14	0.4%

4.7.3 Minimum Age model

The decision was made to use an unlogged version of the 3-parameter Minimum Age Model (MAM3_{ul}) (Galbraith et al, 1999; Arnold et al., 2009), as our data showed negative D_e-values due to the very young age of the sediment.

As the minimum age model puts more emphasis on the right side (lower values) of the D_e-distribution, it is likely that quartz grains from the upper part of the tube are overrepresented in the final result. Therefore the decision was made to make a correction on the sampling depth using the formula; *Sampling depth* – 0.5 * *r_{tube}* rounded off to 0.5 centimetres for convenience. This meant that for samples NR-1 to NR-10 the depth used for MAM3_{ul} outcomes was lowered by 0.5 cm, NR-11 and NR-12 -1 cm, NR-13 -1.5 cm and NR-14 -2 cm.

Overdispersion and model sensitivity

The minimum age model needs an indication of the expected overdispersion in order to properly calculate D_e values. The overdispersion is a measure of the spread of within the D_e values of the sample. This dispersion is input in the model as the parameter σ_b . In order to get a proper value for σ_b , the choice was made to calculate the overdispersion (Table 5) and its error in the 14 different samples using the unlogged version of the Central Age Model (CAM_{ul}) and then use this as an input for the MAM3_{ul}. To get reliable results, we treated the oldest sample (NR-14) from this dataset as an outlier, as it had an overdispersion of 0.004, which was much lower than the average (0.33) and about three times lower than the second lowest value (0.004 vs. 0.011). To check the method for sensitivity of initial starting values, the MAM3_{ul} was run with the same overdispersion input for multiple starting values of σ_b (Table 6). With this input, the MAM3_{ul} gave values of 0.11 +/- 0.09. This value was then used as input parameter σ_b in the further analysis.

Table 6: σ_b sensitivity of the MAM3_{ul}.

σ_b -input	σ_b -output	Error
0.00	0.11	0.09
0.05	0.11	0.09
0.10	0.12	0.09
0.15	0.12	0.09
0.20	0.12	0.10
0.25	0.12	0.09
0.30	0.13	0.10

Model iteration

The Minimum Age Model also needs an expected equivalent dose to properly produce values. An iterative approach was used. This means that the model was run a first time with a linear approximation of the ages as expected equivalent dose. For this linear estimate the surface was taken as age 0 and the depth of what is expected to be the transition from a sandy coastal plain into a salt marsh at 48.5 centimetre depth as 130 years old. This was then multiplied with an expected average DR value of $1.2 \cdot 10^{-3}$ Gy/y to come to expected equivalent doses. Then the model was run twice more, with the output from the previous run as input for the expected dose rate.

Bootstrapping and Likelihood functions

Cunningham and Wallinga (2012) have developed a statistical protocol for potentially poorly bleached sediments in fluvial deposits of relative young age, in a way similar to the situation faced in this research. By using a combination of bootstrap likelihoods and Bayesian processing, they have tried to further improve age models by taking uncertainty from both the sensitivity of the age model to separate aliquots and/or grains and the assumed width of the population of well-bleached (completely reset) grains into account. The uncertainty distributions of different samples have to overlap, which calls for a high sampling resolution.

Bootstrapping is a method based on random sampling with replacement, allowing the estimation of the distribution of sampling data. The basics behind bootstrapping are that the sampled data is seen as the true population. By resampling with replacement of this known 'man-made' population, a new 'bootstrap' sample is created with the same n . As the resampling is done with replacement, each of the new bootstrap samples will be different. In this research, this was done 2000 times for each sample, in which the bootstrap mean for each of the samples is computed. The combination of all these bootstrap means will then form a new distribution.

The bootstrapped D_e values were afterwards used for creating likelihood functions for each of the samples. A likelihood function is a function describing a parameter, in this case the equivalent dose, for a given outcome. For the polynomial smoothing applied to the pairs of bootstrap replicate and its likelihood estimate a degree of fit of 6 was used and an unshared systematic error of 0.035 was assumed. The outputs are generated in a probability density function (PDF).

Due to limitations of the model, it was not possible to take the random errors on Dose rate values into account, thus all errors were seen as systematic error and re-added after OxCal outcomes.

4.8 Dose Rate determination

Normally the outer sides of the sampling tubes, which are not used for D_e -determination to prevent the effect of bleaching during sampling are used for DR-determination as this is the most local material and thus gives the best indication of the received ionising radiation for the D_e -samples, or the gamma radiation has to be measured on-site, to counter the effect of non-homogeneity on DR calculation. For this same reason, it is recommended to take OSL-samples from larger homogeneous layers (Preusser et al., 2008).

As the upper part of our sampling location consisted of a lamination of different soil texture classes, with a whole range of contrasting Dose rates, it was not possible to take samples from a homogenous layer except from the lower part (below the boundary at 51 cm) of the profile. It was also not plausible to use the material from the small diameter metal tubes as these were unlikely to yield enough material and were taken specifically from the more sandy layers, which would have resulted in a systematic underestimation of DR-values and thus an overestimation of ages for the upper part of the profile.

In this research, there were six separate DR samples taken (Table 7, NR-A to NR-F), which had to be adjusted in order to make a correct estimate of the *in-situ* DR-values. For the underlying, more massive layers the DR was determined with material from the same tube as the D_e - samples (Table 7, NR-11 to NR-14).

For DR determination all samples were weighed, heated to 105 °C to determine water content and afterwards ashed for 24 hours at 500 °C to determine the organic material as Loss on Ignition (LOI). The remaining material was grinded and consequently mixed with wax to make 2 cm thick pucks for high resolution gamma-ray spectrometry. To calculate DR-values, the conversion factors from Guérin et al. (2011) were used. For the cosmic DR Prescott & Hutton (1994) was followed and a shallowness correction assuming gradual burial based on Madsen (2005) was applied. For the internal alpha a standard value of 0.010 ± 0.005 (Vandenbergh et al., 2008) was used.

Table 7: Measured water content, Loss on Ignition, un-attenuated beta Dose Rate (Gy/ka) and un-attenuated gamma Dose Rate (Gy/ka) of samples NR-A to NR-F and NR-11 to NR-14.

Sample #	Depth below surface (cm)	NAP (m)	Measured Water content (%)	Measured Loss On Ignition(%)	Unattenuated beta (Gy/ka)	Error	Unattenuated Gamma (Gy/ka)	Error
NR-A	12	+1.39	32.09	7.31	1.86	0.07	1.16	0.05
NR-B	19	+1.32	32.56	6.03	1.76	0.07	1.09	0.04
NR-C	24	+1.27	33.67	5.80	1.62	0.06	0.95	0.04
NR-D	31	+1.20	20.01	2.51	1.15	0.05	0.63	0.03
NR-E	36	+1.15	16.09	1.20	0.98	0.04	0.51	0.02
NR-F	41	+1.10	17.37	1.49	1.11	0.05	0.59	0.03
NR-11	48	+1.03	30.98	3.94	1.71	0.07	0.94	0.04
NR-12	54	+0.97	8.10	0.47	1.14	0.05	0.74	0.03
NR-13	63	+0.88	7.67	0.27	0.92	0.04	0.55	0.03
NR-14	79	+0.72	12.34	0.24	0.73	0.03	0.34	0.02

4.8.1 Attenuation factors

Both the LOI, as the water content influence the attenuation of both beta and gamma radiation in soils. During the preparation of the DR samples these are normally both measured and can be applied directly to the unattenuated DR's and age determination. As for most of our samples the D_e and DR are determined from different tubes, a couple of interpolations had to be made for both organic matter content as the water content to determine the received radiation for all D_e -samples (Madsen et al., 2005).

Water content

Determining an average water content was challenging for an area under direct influence of the sea, and thus under a continuously varying water level. More than anything, the measured water contents (Table 7) reflect the earlier mentioned lithology of the profile. There is a fining upward sequence in the salt marsh part, in which the more clay dominated upper part of the profile retains more water and drains less easily than the more sandy lower part. Also the clayey layer just above the sharp defined boundary with the lower lying overwash plain deposits, from which sample NR-11 was taken, has a high water content. When we compare the measured values to the typical values for the different texture classes, it seems that all samples are at or near field capacity, which is the state soils typically are a couple of days after wetting, when free draining has stopped (Dunne and Leopold, 1978). The three lowest samples, which are part of the underlying massive sand, are likely to drain rapidly explaining their low water contents. Finally, the measured values were taken as the best possible estimate, with an error-estimation of 25%.

Organic matter content

The organic matter content in the DR-samples was measured as the Loss on Ignition (LOI), after ashing the samples at 500 °C for 20 hours. The difference in weight before and after the ashing procedure was assumed to be the organic matter content of the sample. An error of 10% was assumed.

4.8.2 Beta Dose rate

Since beta radiation has a very limited penetration depth of around 2-3 mm (Aitken, 1985) and the sand which was measured stems mainly from sandy layers which were thicker than that, it seems to be a reasonable assumption to take the unattenuated beta dose rate from the DR sample NR-E (0.98 Gy/ka) with a typical 4% error. NR-E was taken from the same, 3 centimetre thick, relative clean layer of sand as D_e sample NR-8 (see Table 1 for soil description). This sand-dominated sample is likely to be best mimicking the unattenuated beta DR as received within the sandy layers of the profile. The other DR samples were taken either from too clay dominated parts of the profile and the unattenuated beta DR's from the underlying massive sands are likely to be too low, as the amount of clay there is likely to be lower than within the measured sandy layers.

Beta dose rate attenuation

After determining the external beta Dose rate, the attenuation factors for the beta Dose rate had to be estimated. As the sandy layers are confined between more clayey/loamy material which tends to better retain water than more sandy samples, the assumption was made that the amount of water attenuating radiation is likely to follow the overall trend within the profile. Therefore, a linear estimation was made between the known water contents of the DR-samples to find water content estimates for the D_e-sample depths.

For the LOI within the sandy layers, it seems reasonable that the values are similar to the ones in sample NR-E, which is also the sample from which the beta DR was taken as best estimate. Therefore, a LOI-value of 1.20% with an error of 10% was taken as a best estimate.

Table 8: Un-attenuated beta Dose Rate per sample, water content estimate per sample, LOI estimate per sample and attenuated beta Dose Rate per sample

NR- #	Unattenuated beta (Gy/ka)	Error	Water content (%)	Error	LOI (%)	Error	Attenuated beta (Gy/ka)	Error
1	0.980	0.041	32.09	8.02	1.20	0.73	0.614	0.054
2	0.980	0.041	32.09	8.02	1.20	0.73	0.614	0.054
3	0.980	0.041	32.22	8.06	1.20	0.69	0.613	0.054
4	0.980	0.041	32.56	8.14	1.20	0.60	0.611	0.054
5	0.980	0.041	33.34	8.33	1.20	0.59	0.607	0.054
6	0.980	0.041	24.89	6.22	1.20	0.37	0.655	0.049
7	0.980	0.041	18.83	4.71	1.20	0.21	0.695	0.045
8	0.980	0.041	16.48	4.12	1.20	0.13	0.712	0.044
9	0.980	0.041	16.86	4.21	1.20	0.14	0.709	0.044
10	0.980	0.041	23.20	5.80	1.20	0.25	0.666	0.048
11	1.709	0.068	30.98	7.75	3.94	0.39	1.055	0.087
12	1.140	0.046	8.10	2.09	0.47	0.05	0.913	0.043
13	0.923	0.038	7.67	1.92	0.27	0.03	0.744	0.035
14	0.733	0.031	12.34	3.09	0.24	0.02	0.562	0.031

4.8.3 Gamma Dose Rate

Using the general attenuation factors for gamma radiation in soil from Aitken (1985), it was possible to construct the following graph (Figure 14, pers. comm. N. Hobo, 2016) to model the received gamma radiation for each depth in the soil profile. As input the water, organic matter (Aitken, 1998) and grain size (Mejdahl, 1979) attenuated received gamma radiation was used. For gamma Dose rate from the underlying area, the gamma DR of the lowest sample (NR-14, 79 cm) was taken.

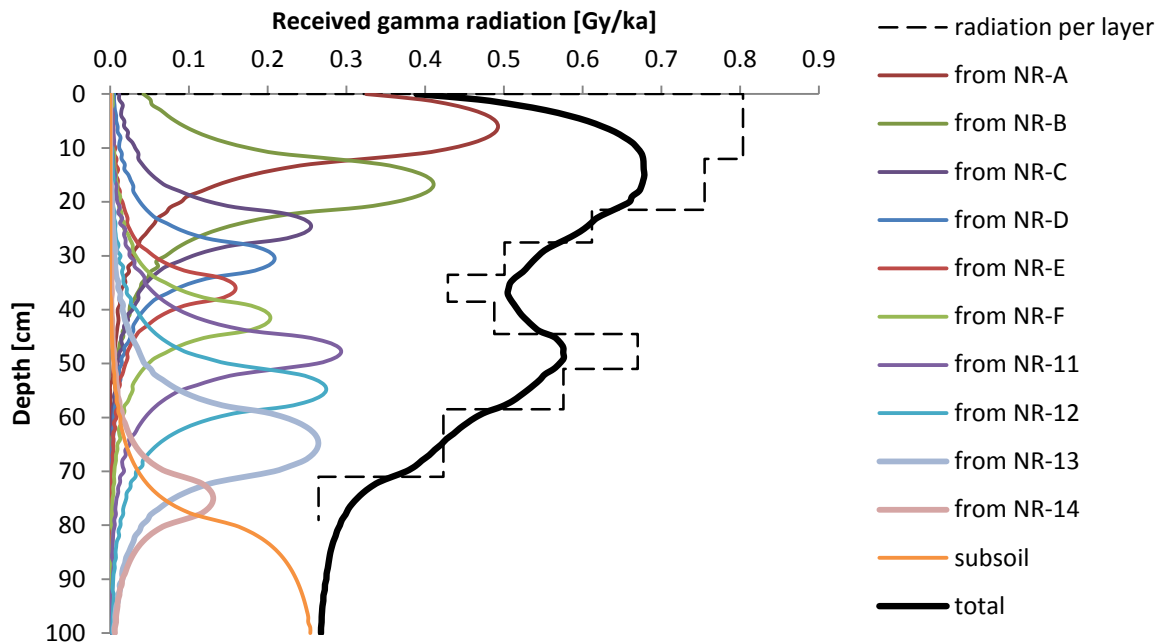


Figure 14: Interpolated gamma radiation per layer (pers. com. N. Hobo).

As the depth for the samples was adjusted for the minimum age (in this case dose) model, the final DR-values differed slightly between the minimum age model and the iterative model.

4.9 OxCal model

After determining the ages by dividing the equivalent dose data through the determined DR-values, the free to use tool OxCal was used. OxCal is a chronological tool which uses Bayesian statistics to improve the dating of sedimentary sequences (Bronk Ramsey, 1995). For the input of the data from this research the P_Sequence was used. This sequence based on the assumption that deposition follows a random Poisson process, in which every moment of deposition is a random event (Bronk Ramsey, 2008). This best mimics the random nature of deposition on a salt marsh, as this is mainly governed by events when the salt marsh is submerged. All inputs in the OxCal sequence were applied using only the random error, as this is a prerequisite of the program. The choice was made to take a k-value of 1000, describing the amount of events per meter and 50 automatically generated depth model points per meter. As the value of k can vary between depositional events in order of magnitude, a prior for $\log_{10}(k/k_0)$ in the form of a uniform PDF with boundaries of -1.5 and 1.5 was defined. This allows variation of one and half order of magnitude in either direction, therewith covering both the more than centimetre-scale thickness of the sandy layers and the very fine lamination of the more clayey deposits within the profile.

As OxCal takes all the samples in the sedimentary sequence into account, sample age have to be input with only their random errors. As systematic errors are the same for each of the samples, taking these into account as well would lead to an overestimation of the final error per sample.

5. Results

5.1 Results of the D_e measurements

After analysing all the raw data with the Analyst tool, using the settings mentioned, the D_e -samples yielded the following equivalent dose distributions (Figure 15 and 16). The graphs show the D_e -distributions of the data, as well as the standard error. It is clear that many of the distributions show a non-Gaussian form with a longer tail on the right side of the distribution. This is also represented in the skewness and kurtosis-scores.

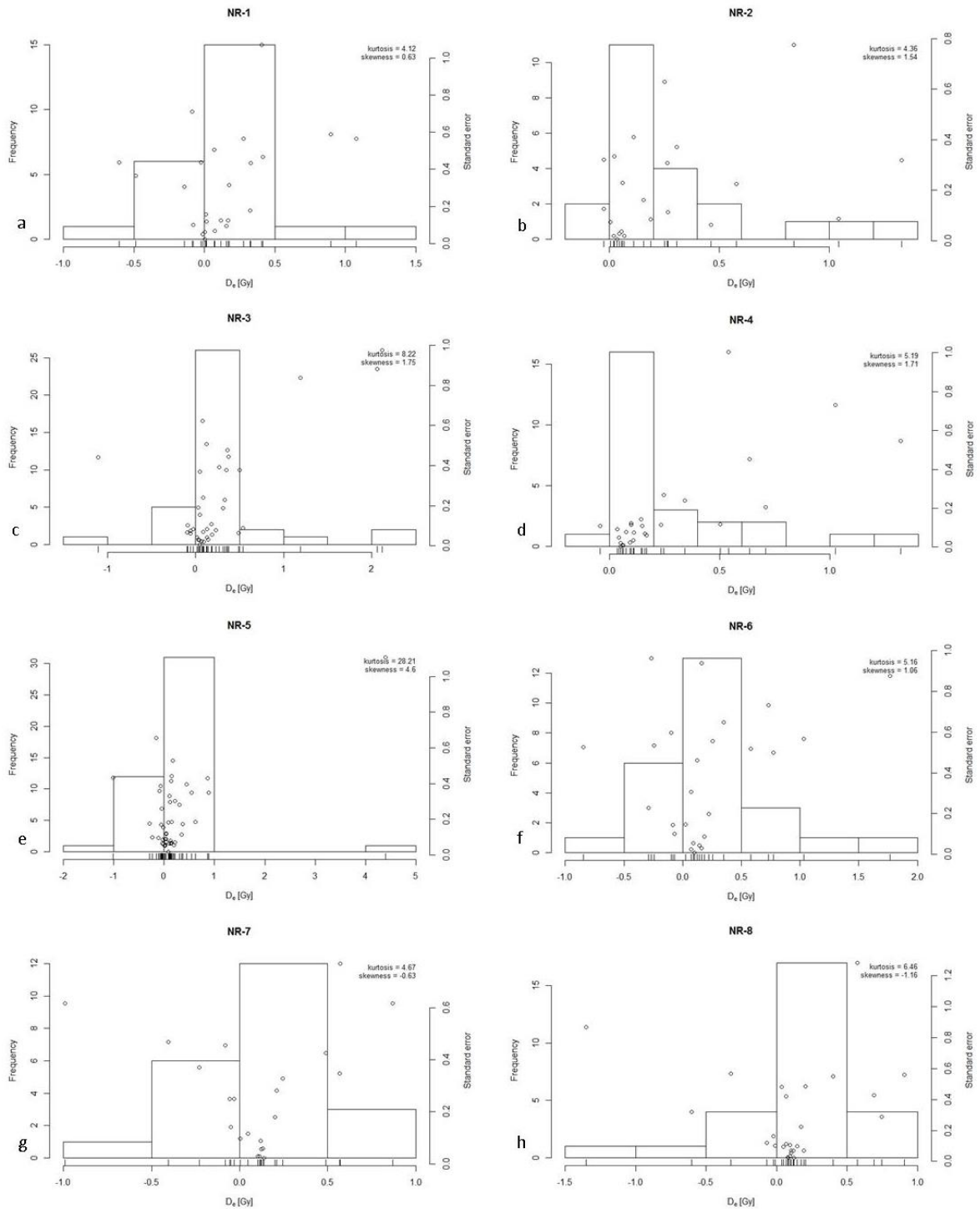


Figure 15: Equivalent dose distributions of samples NR-1 to NR-8.

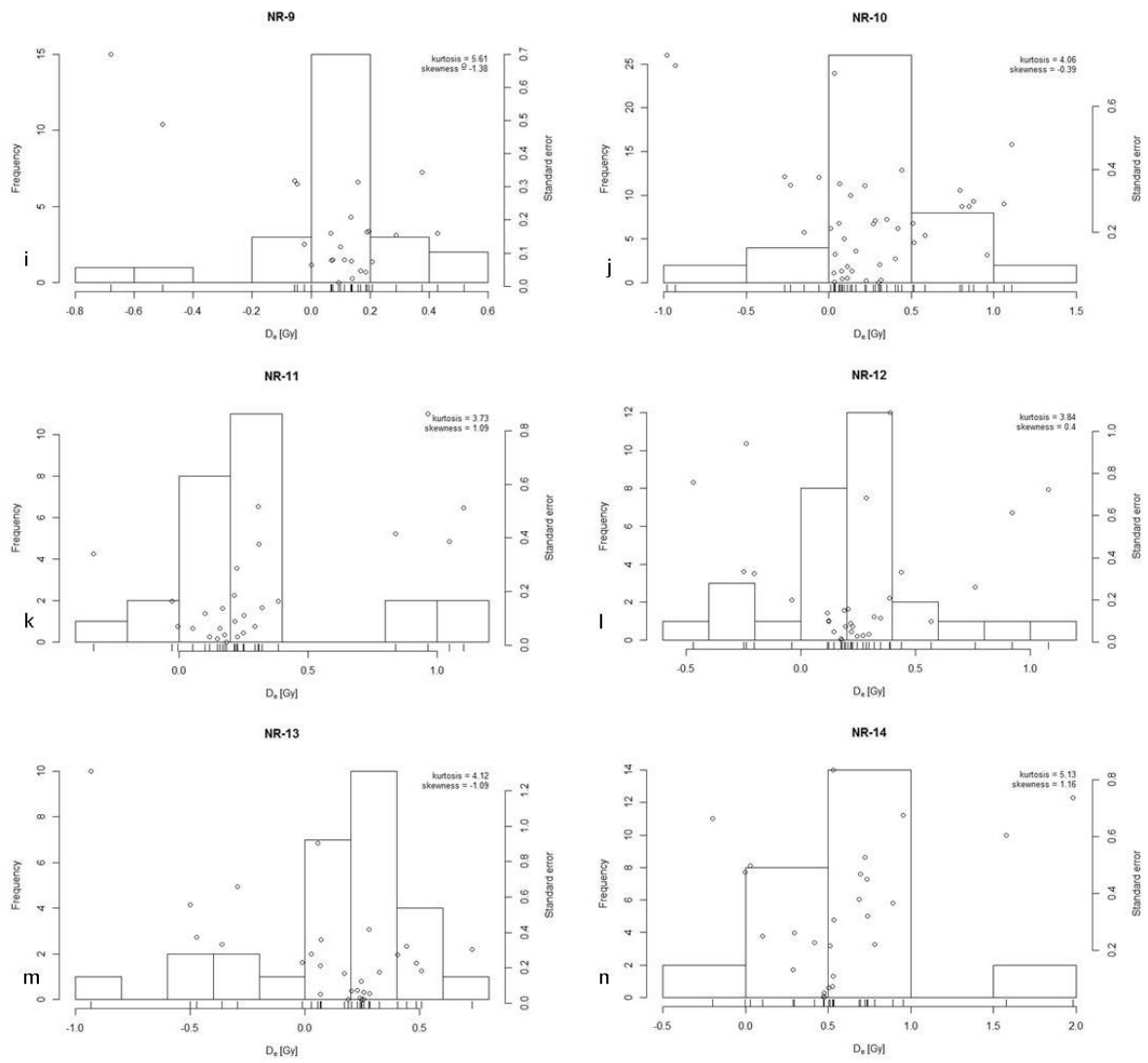


Figure 16: Equivalent dose distributions for sample NR-9 to NR-14.

5.2 Bleaching indicators

In the upper part there are multiple indicators for poor bleaching (Table 9). The Poor Bleaching scores, as defined by Cunningham et al. (2015), are relatively high. Also the overdispersion for the samples in the upper part of the profile, determined using the unlogged Central Age Model (Arnold et al., 2009), are higher than in the lower part of the profile. Another indicator is the difference between the modelled outcomes of the CAM_{ul} and the MAM3_{ul}. In perfect conditions, the outcomes of both models are almost similar. This is due to the way both models treat the distribution of doses within the samples. In poorly bleached samples, there is a peak somewhere in the lower part of the distribution, with an extended tail towards the higher equivalent doses. The Minimum Age Model aims for the left part of this distribution, thereby lowering the weight of the higher dose points. The Central Age Model gives most weight to the centre of the distribution. In case of perfect bleaching, the equivalent dose distribution follows a Gaussian distribution and therefore both models would give equal outcomes.

5.2.1 Skewness

Skewness is a value describing the shape of the distribution of the data. Negative values indicate that the mass of the distribution is concentrated on the left side and positive values indicate a concentration of mass on the right side. A Gaussian normal distribution has a skewness of zero. For most samples in this research the skewness scores are positive, with samples NR-2, 3, 4 and 5 showing skewness scores of above 1.5, with a maximum of 4.6 for sample NR-5. Samples 7, 8, 9, 10 and 13 showed slight negative skewness values, varying between -0.39 and -1.38. This can be an indication of bioturbation, which is the reworking of sediments after deposition through biological activity (Madsen et al., 2011).

5.2.2 Kurtosis

Similar to the before mentioned skewness, kurtosis is a descriptor of the shape of the probability distribution. The given value is therefore a description of the tails of the distribution and not its peak. A Gaussian normal distribution has a kurtosis of 3. Lower values indicate that the distribution has a lower amount and less extreme outliers, where high values are an indication of outliers. Samples NR-1, 2, 7, 10, 11, 12 and 13 show kurtosis-values of below 5. Again NR-5 has the highest value, with a kurtosis value of 28.21.

Table 9: Bleaching indicators; overdispersion, skewness, kurtosis and difference between equivalent doses from the unlogged Central Age Model and unlogged 3-parameter Minimum Age Model.

NR-#	Poor Bleaching Score (Cunningham et al., 2015)	Overdispersion (%)	Skewness	Kurtosis	Difference CAM _{ul} -MAM3 _{ul}
1	0.058	56.6%	0.63	4.12	0.211
2	0.259	63.8%	1.54	4.36	0.370
3	0.189	56.4%	1.75	8.22	0.274
4	0.143	37.7%	1.71	5.19	0.202
5	0.198	70.1%	4.60	28.21	0.404
6	0.066	26.3%	1.06	5.16	0.144
7	0.016	1.1%	-0.63	4.67	0.004
8	0.027	21.2%	-1.16	6.46	0.031
9	0.096	12.5%	-1.38	5.61	0.043
10	0.380	60.0%	-0.39	4.06	0.336
11	0.159	22.8%	1.09	3.73	0.138
12	0.137	21.9%	0.40	3.84	0.095
13	0.147	10.7%	-1.09	4.12	0.052
14	0.055	0.4%	1.16	5.13	0.063

5.3 Iterative model outcomes

After running the iterative cycle five times, the remaining aliquots were averaged to come to D_e -values for each of the samples. The amount of remaining aliquots and the averaged D_e -values are presented in Table 10.

Table 10: Number of tested aliquots per sample, luminescent aliquots per sample, number of accepted aliquots for the iterative model and the averaged D_e -values.

NR-#	Number of luminescent aliquots per sample	Number of accepted aliquots in iterative model	Percentage of accepted aliquots	Averaged D_e	Total D_e error
1	24	14	58%	0.042	0.023
2	22	13	59%	0.055	0.018
3	37	22	59%	0.075	0.016
4	26	16	62%	0.094	0.011
5	45	28	62%	0.058	0.014
6	25	12	48%	0.107	0.023
7	22	13	59%	0.081	0.025
8	27	14	52%	0.096	0.010
9	25	15	60%	0.136	0.013
10	42	23	55%	0.151	0.023
11	26	13	50%	0.203	0.014
12	30	18	60%	0.216	0.017
13	28	16	57%	0.198	0.022
14	26	15	58%	0.570	0.031
Sum	405	232	57%		

5.4 Bootstrap likelihood functions

Here presented are the likelihood functions of the bootstrapped, 3-parameter minimum age model (Cunningham and Wallinga, 2012) in the form of probability density functions. The bootstrapped likelihood procedure was able to create a nice fit for most of the samples (Figure 17 and 18). Only sample NR-5 (Figure 17-e) turned out poorly, but this was no surprise given the high skewness and kurtosis factors (4.6 and 28.21 respectively) established earlier (Table 9).

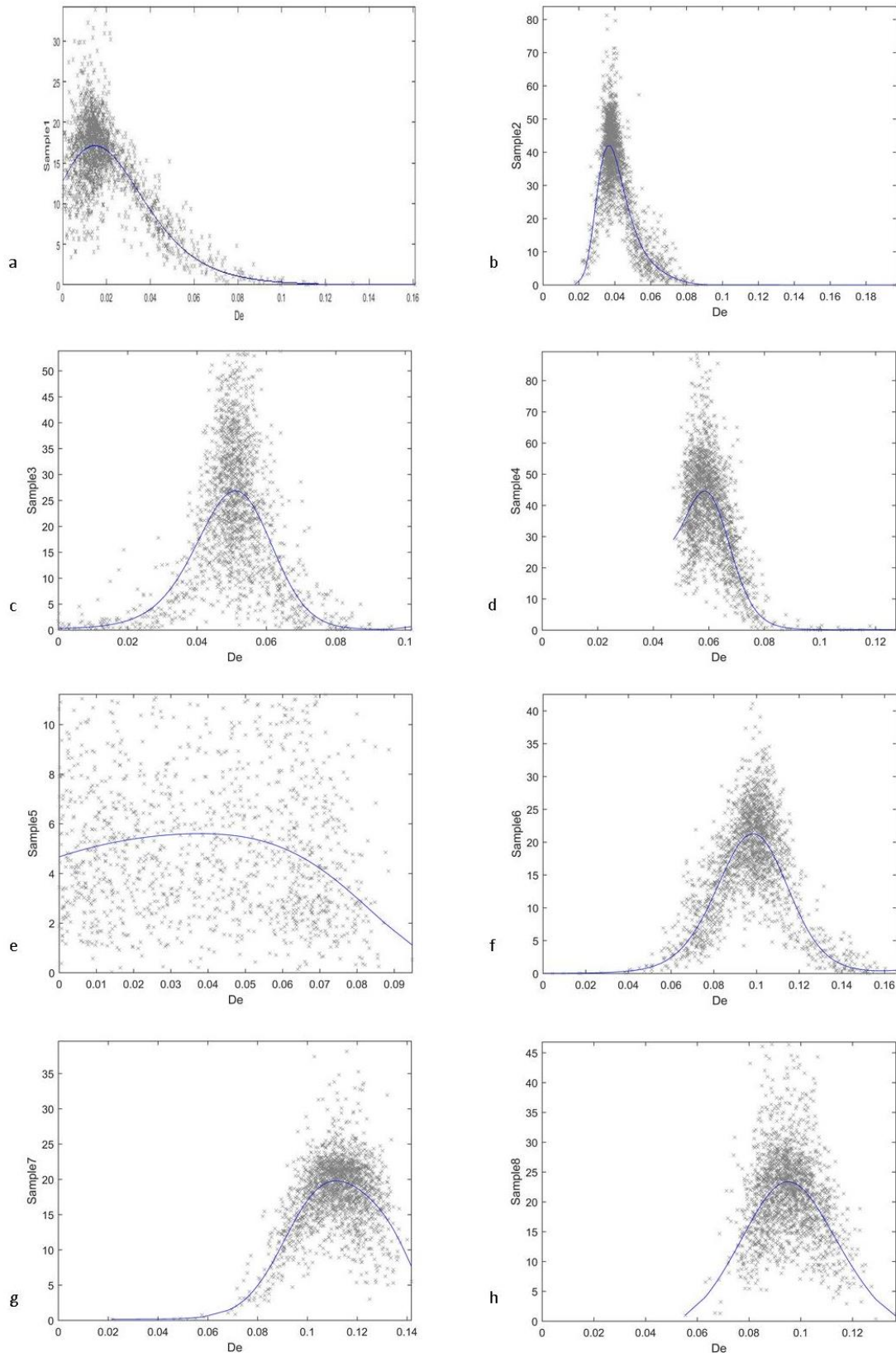


Figure 17: Probability Density Functions of bootstrapped likelihoods of sample NR-1 to NR-8.

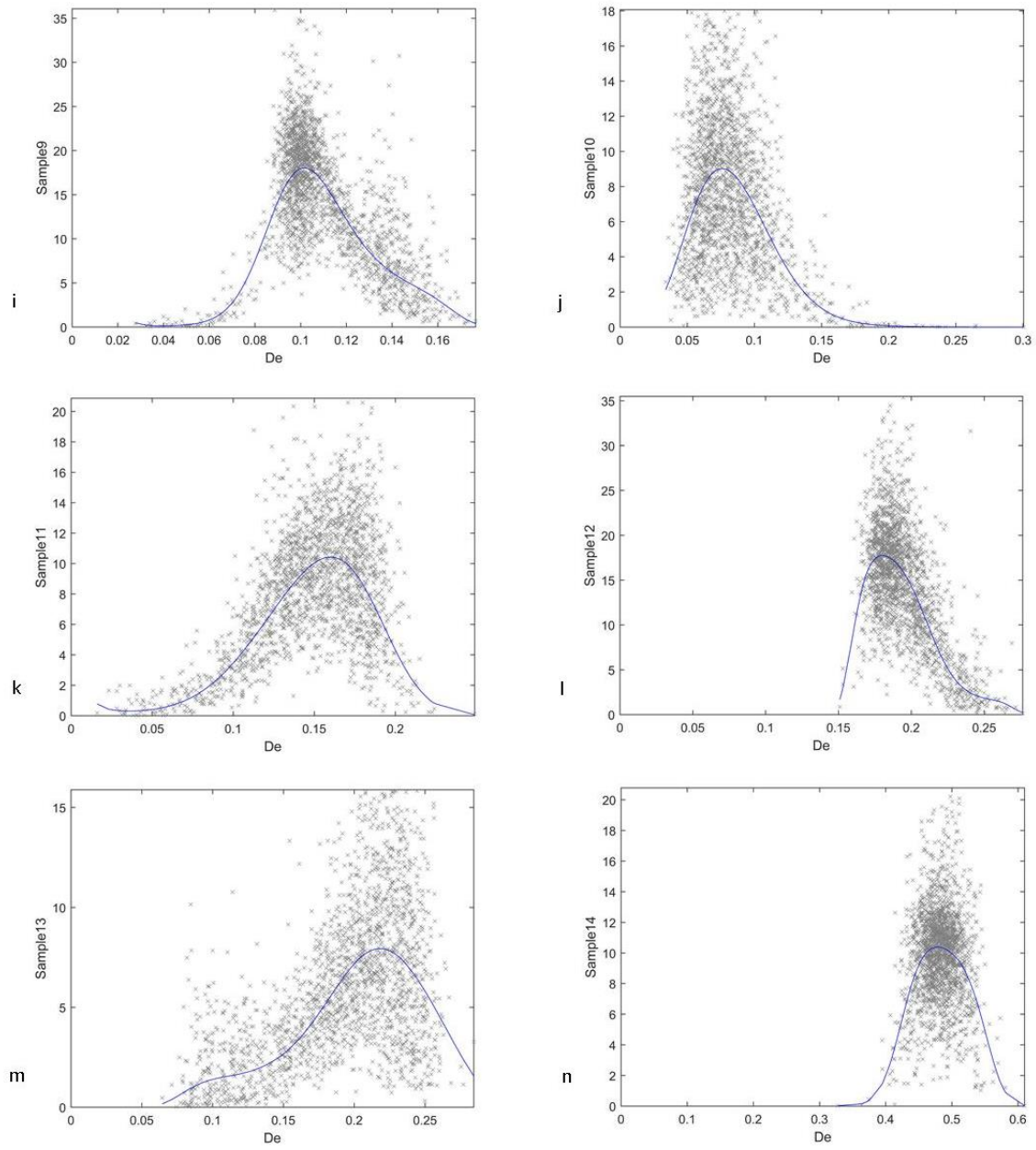


Figure 18: Probability Density Functions of bootstrapped likelihoods of sample NR-9 to NR-14.

5.5 Equivalent Doses according to different age models

The found equivalent dose data was then further analysed using the three different age (in this case equivalent dose) models. The results of the Central Age Model, the Iterative model and the 3-parameter Minimum Age Model are presented in Table 11.

Table 11: Equivalent Dose outcomes of the unlogged Central Age Model (CAM_{ul}), the Iterative model and the unlogged 3-parameter Minimum Age Model ($MAM3_{ul}$)

NR-#	Depth (original)	Iterative model		CAM_{ul}		Depth ($MAM3_{ul}$)	$MAM3_{ul}$	
	(cm)	D_e (Gy)	Error	D_e (Gy)	Error	(cm)	D_e (Gy)	Error
1	3.5	0.042	0.023	0.232	0.168	3.0	0.021	0.016
2	9.0	0.055	0.018	0.413	0.130	8.5	0.043	0.011
3	14.0	0.075	0.016	0.316	0.119	13.5	0.042	0.030
4	19.0	0.094	0.011	0.262	0.090	18.5	0.061	0.007
5	22.5	0.058	0.014	0.426	0.249	22.0	0.022	0.042
6	28.5	0.107	0.023	0.239	0.134	28.0	0.095	0.019
7	32.5	0.081	0.025	0.116	0.068	32.0	0.112	0.011
8	35.5	0.096	0.010	0.126	0.090	35.0	0.094	0.009
9	39.0	0.136	0.013	0.154	0.034	38.5	0.111	0.022
10	44.0	0.151	0.023	0.415	0.079	43.5	0.079	0.027
11	48.5	0.203	0.014	0.285	0.074	47.5	0.147	0.034
12	54.5	0.216	0.017	0.289	0.039	53.5	0.193	0.017
13	63.0	0.198	0.022	0.247	0.028	61.5	0.195	0.045
14	79.0	0.570	0.031	0.545	0.067	77.0	0.482	0.019

5.6 Dose Rates

The interpolations for the external gamma dose and the estimate for the beta dose rate, combined with the attenuation factor lead to the following DR-values for the different samples (Table 12). As a depth correction had been carried out for the MAM3_{ul}, the estimated Dose rate also had to be adjusted accordingly (Table 13).

Table 12: Separate Dose Rate contributions per sample (Gy/ka).

NR-#	Internal alpha (Gy/ka)	Error	Wet attenuated beta (Gy/ka)	Error	Wet attenuated gamma (Gy/ka)	Error	Cosmic dose rate (Gy/ka)	Error	Total Dose Rate (Gy/ka)	Error
1	0.010	0.005	0.614	0.054	0.568	0.034	0.287	0.014	1.479	0.065
2	0.010	0.005	0.614	0.054	0.663	0.038	0.282	0.014	1.569	0.068
3	0.010	0.005	0.613	0.054	0.678	0.040	0.277	0.014	1.578	0.068
4	0.010	0.005	0.611	0.054	0.664	0.039	0.273	0.014	1.558	0.068
5	0.010	0.005	0.607	0.054	0.627	0.038	0.270	0.013	1.513	0.068
6	0.010	0.005	0.655	0.049	0.561	0.032	0.265	0.013	1.491	0.060
7	0.010	0.005	0.695	0.045	0.532	0.029	0.262	0.013	1.498	0.055
8	0.010	0.005	0.712	0.044	0.513	0.028	0.259	0.013	1.494	0.053
9	0.010	0.005	0.709	0.044	0.521	0.028	0.257	0.013	1.497	0.054
10	0.010	0.005	0.666	0.048	0.560	0.031	0.253	0.013	1.489	0.059
11	0.010	0.005	1.055	0.087	0.603	0.037	0.250	0.013	1.919	0.096
12	0.010	0.005	0.913	0.043	0.599	0.028	0.246	0.012	1.769	0.053
13	0.010	0.005	0.744	0.035	0.503	0.025	0.241	0.012	1.498	0.045
14	0.010	0.005	0.562	0.031	0.334	0.019	0.233	0.012	1.138	0.038

Table 13: Estimated Dose Rates (Gy/ka) for the different models.

NR-#	Depth (original)	Dose rate estimate for CAM _{ul} and Iterative model		Depth (MAM3 _{ul})	Dose rate estimate for MAM3 _{ul}	
	(cm)	Gy/ka	Error	(cm)	Gy/ka	Error
1	3.5	1.448	0.061	3.0	1.433	0.061
2	9.0	1.537	0.064	8.5	1.532	0.064
3	14.0	1.549	0.065	13.5	1.549	0.065
4	19.0	1.533	0.065	18.5	1.537	0.065
5	22.5	1.489	0.065	22.0	1.496	0.065
6	28.5	1.476	0.059	28.0	1.482	0.059
7	32.5	1.492	0.055	32.0	1.495	0.055
8	35.5	1.493	0.053	35.0	1.494	0.053
9	39.0	1.495	0.054	38.5	1.493	0.054
10	44.0	1.481	0.058	43.5	1.476	0.058
11	48.5	1.920	0.096	47.5	1.916	0.096
12	54.5	1.770	0.069	53.5	1.775	0.069
13	63.0	1.500	0.057	61.5	1.341	0.052
14	79.0	1.140	0.055	77.0	1.140	0.055

5.7 Ages for the different models

After defining the D_e -values through the different age-models, to be more exact equivalent dose models, the equivalent doses had to be divided through their respective DR-estimates to come to ages (Table 14, Figure 19), errors were propagated using a numerical approach. The boundary seen in the profile is also added as an independent age control of around 1890 at a depth of 51 cm.

Table 14: Outcomes of the unlogged Central Age Model (CAM_{ul}), the iterative model and the 3-parameter Minimum Age Model ($MAM3_{ul}$).

NR-#	Depth (original)	Iterative model		CAM_{ul}		Depth ($MAM3_{ul}$)	$MAM3_{ul}$	
	(cm)	Age (AD)	Error	Age (AD)	Error	(cm)	Age (AD)	Error
1	3.5	1987.9	16.1	1855.9	116.1	3.0	2001.6	11.4
2	9.0	1981.1	11.6	1747.2	85.0	8.5	1987.9	7.1
3	14.0	1968.8	10.5	1812.0	77.5	13.5	1988.9	19.3
4	19.0	1955.7	7.6	1844.9	58.9	18.5	1976.5	4.6
5	22.5	1978.3	9.8	1729.8	167.6	22.0	2001.2	28.3
6	28.5	1944.5	15.8	1853.8	91.1	28.0	1951.9	13.1
7	32.5	1962.8	16.9	1938.4	45.8	32.0	1941.4	7.6
8	35.5	1952.8	7.2	1931.8	60.3	35.0	1952.8	6.4
9	39.0	1926.1	9.1	1913.0	23.2	38.5	1941.6	14.9
10	44.0	1915.3	16.0	1735.6	54.7	43.5	1962.5	18.4
11	48.5	1911.5	9.0	1867.7	39.5	47.5	1939.5	18.0
12	54.5	1895.1	10.6	1852.8	22.7	53.5	1907.0	10.7
13	63.0	1884.8	15.7	1851.5	19.5	61.5	1870.9	34.2
14	79.0	1516.6	36.4	1538.1	63.5	77.0	1593.3	26.4

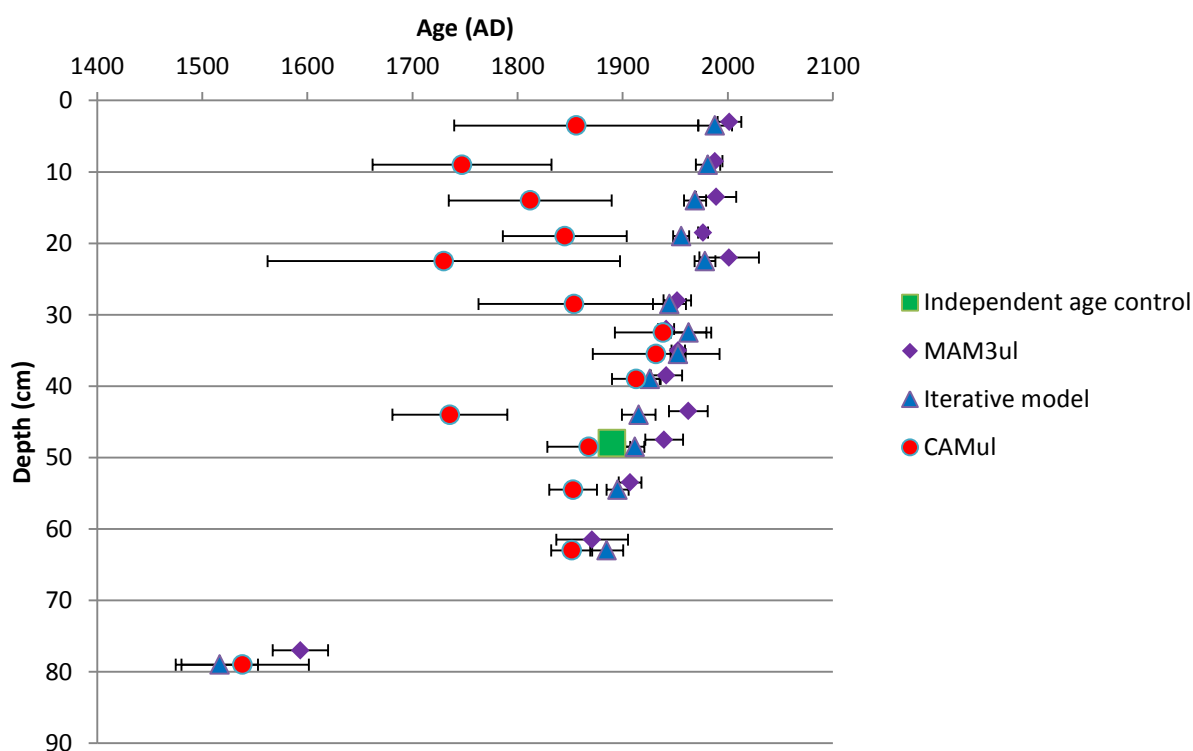


Figure 19: Outcomes of different age models plotted versus depth. Iterative model, .Unlogged Central Age Model (CAM_{ul}) and unlogged 3-parameter Minimum Age Model ($MAM3_{ul}$).

5.8 Choice of appropriate model

Before making a decision on the outcomes of which age model (Iterative model, CAM_{ul} and bootstrapped likelihood MAM3_{ul}, Table 14) are to be used for further analysis of the accretion speed, the three different age models need to be carefully compared.

The CAM_{ul} outcomes show very large uncertainties in the upper part of the profile, as well as being stratigraphically inconsistent. The likely cause for this is that the Central Age Model is too sensitive for poorly bleached aliquots and therefore gives overestimations of the equivalent doses and thus ages. As it is a weighted model it gives more weight to samples of older age, as the relative error on aliquots with higher doses is lower due to a lower signal to noise ratio (Madsen and Murray, 2009). The large errors in the output are due to the incapability of the model to handle the large scatter associated with the poorly bleached samples of the upper part of the profile (Table 9). For these reasons, it was not taken into account for further analysis

The bootstrapped likelihood MAM_{ul} outcomes seem stratigraphically consistent, but the model tends to put more emphasis on the left side of the equivalent dose distribution, which makes it more sensitive to low outliers. This can lead to an underestimation of the ages, especially combined with the negative skewness values of samples NR-7 to NR-10 (Table 9), which potentially indicate bioturbation. Also NR-11 (1939.5±18.0, 47.5 cm depth), seems to slightly contradict, what is thought to be the independent age control of around 1890 at around 51.0 cm depth, also when we take the 2-sigma uncertainty. The complexity of the model is also a disadvantage, as there are multiple assumptions that are made when building the model.

The Iterative model is less affected by outliers in both positive as negative directions. Therefore, it is very suited for samples with a negative skewness factor, such as samples NR-7 to NR-10 and sample NR-13, and also handles samples with a large positive skewness and a couple of large positive outliers (Table 9). Cases with many poorly bleached grains, in which much of the D_e-distribution is shifted towards higher D_e-values, the Iterative model can give an overestimation of D_e-values, leading to an overestimation of ages. Overall, the outcomes of the Iterative model seem stratigraphically consistent.

As both the bootstrapped likelihood MAM3_{ul} as the Iterative model show stratigraphically consistent outcomes, for both the stratigraphical consistency was analysed with OxCal.

5.9 OxCal outputs

As OxCal takes the depth and relative position compared to other measurements into account as a prior for Bayesian statistics, it can be used to check consistency of the samples within the profile. The best fits for the Iterative model were achieved when, in addition to the boundary in the profile at 51 cm, an additional boundary between sample NR-14 and NR-13 was added and sample NR-5 was removed.

It seems reasonable to add an extra boundary between the two lowest samples, as these stem from different time periods. Downside to this was that OxCal was not able to make a sequence out of a single data point, in this case NR-14. Also removing sample NR-5 for the sake off overall model fit seems correct, given its skewness (4.60), kurtosis (28.21), overdispersion (70.1%), difference between the CAM_{ul} and MAM3_{ul} (0.404 Gy, Table 12) and the shape of the likelihood function (Figure 12-e). The boundary that was clearly seen in the profile at 51 cm depth (Table 1, Figure 3, 7 & 8) was included in both models as a 'top-hat' distribution with an expected date of 1890 and a 1-σ uncertainty of 5 years.

The OxCal model produces output in Agreement indices, which in general should all be above 60%. 'A' is the measure of whether an individual sample agreement with the model, 'A_{overall}' is a product of the individual agreement indices and 'A_{model}' indicates whether the model as a whole is likely given the input data.

The bootstrapped likelihood MAM3_{ul} produced an A_{overall} of 82% and an A_{model} of 89.3%, but with poor agreement on sample NR-10 as the agreement index is only 44.1% (Figure 20). The Iterative model shows the best fit with the given data. The overall fit of the separate data point comes to 101.8% and the model fit to 103.8% (Figure 21 & 22). Therefore, the choice was made to further analyse the accretion speeds with the OxCal Iterative model outcomes.

Name		Unmodelled (BC/AD)			Modelled (BC/AD)			Indices A _{model} =89.3 A _{overall} =82				Select	Page break	
Show all Show structure		from	to	%	from	to	%	A _{comb}	A	L	P	C	All Visible	
► Depth_Model													<input checked="" type="checkbox"/> 37	<input type="checkbox"/>
Page													<input type="checkbox"/>	<input type="checkbox"/>
► Depth_Model													<input checked="" type="checkbox"/> 21	<input type="checkbox"/>
Page													<input type="checkbox"/>	<input type="checkbox"/>
Boundary Top					1995.1	2010.62	68.2					98.3	<input checked="" type="checkbox"/> 20	<input checked="" type="checkbox"/>
Prior NR1		1989.45	2020.21	68.2	1995.1	2010.62	68.2		127.8			98.3	<input checked="" type="checkbox"/> 19	<input type="checkbox"/>
Prior NR2		1984.01	1997.3	68.2	1987.74	1996.37	68.2		118.9			99.6	<input checked="" type="checkbox"/> 18	<input type="checkbox"/>
Prior NR3		1974.27	1991.76	68.2	1978.65	1987.96	68.2		129.1			99.8	<input checked="" type="checkbox"/> 17	<input type="checkbox"/>
Prior NR4		1973.12	1986.03	68.2	1971.25	1980.15	68.2		104.6			99.7	<input checked="" type="checkbox"/> 16	<input type="checkbox"/>
Prior NR5		1966.68	2024.78	68.2	1962.92	1974.39	68.2		101.3			99.9	<input checked="" type="checkbox"/> 15	<input type="checkbox"/>
Prior NR6		1937.1	1962.38	68.2	1949.04	1961.27	68.2		115.8			99.8	<input checked="" type="checkbox"/> 14	<input type="checkbox"/>
Prior NR7		1926.13	1951.93	68.2	1942.43	1954.55	68.2		103.7			99.7	<input checked="" type="checkbox"/> 13	<input type="checkbox"/>
Prior NR8		1940.92	1963.85	68.2	1937.78	1950.39	68.2		101.3			99.4	<input checked="" type="checkbox"/> 12	<input type="checkbox"/>
Prior NR9		1929.11	1960.74	68.2	1929.56	1944.7	68.2		112.8			99.7	<input checked="" type="checkbox"/> 11	<input type="checkbox"/>
Prior NR10		1939.6	1984.68	68.2	1914.8	1934.03	68.2		44.1			99.6	<input checked="" type="checkbox"/> 10	<input type="checkbox"/>
		Warning! Poor agreement - A= 44.1%(A'c= 60.0%)												
Prior NR11		1914.81	1952.07	68.2	1902.05	1919.66	68.2		73.7			99.6	<input checked="" type="checkbox"/> 9	<input type="checkbox"/>
Top_Hat independent age		1885	1895	68.2									<input checked="" type="checkbox"/> 8	<input type="checkbox"/>
▲ Boundary Change		1885	1895	68.2	1891	1894.98	68.2		100			98.4	<input checked="" type="checkbox"/> 7	<input type="checkbox"/>
Prior NR12		1893.75	1920.17	68.2	1880.5	1892.43	68.2		47.9			99.4	<input checked="" type="checkbox"/> 6	<input type="checkbox"/>
		Warning! Poor agreement - A= 47.9%(A'c= 60.0%)												
Prior NR13		1819.58	1884.91	68.2	1809.12	1840.83	68.2		109.4			99.5	<input checked="" type="checkbox"/> 5	<input type="checkbox"/>
Prior NR14		1507.16	1591.47	68.2	1535.11	1616.19	68.2		93.1			98.4	<input checked="" type="checkbox"/> 4	<input type="checkbox"/>
Boundary Bottom					1535.11	1616.19	68.2					98.4	<input checked="" type="checkbox"/> 3	<input type="checkbox"/>
▲ P_Sequence NeerlandsReid		-1.5	1.5	68.2	-1.515	-1.284	68.2		100			98.2	<input checked="" type="checkbox"/> 2	<input type="checkbox"/>

Figure 20: Table output of the bootstrapped likelihoods MAM3_{ul}. All uncertainties are in 1-σ (68.2% certainty).

Name		Unmodelled (BC/AD)			Modelled (BC/AD)			Indices A _{model} =103.8 A _{overall} =101.8				Select	Page break	
Show all												All		
Show structure		from	to	%	from	to	%	A _{comb}	A	L	P	C	Visible	
		Warning! Model not supported in this context - P_Sequence												
► Depth_Model													<input checked="" type="checkbox"/> 35	<input type="checkbox"/>
Page													<input type="checkbox"/>	<input type="checkbox"/>
► Depth_Model													<input checked="" type="checkbox"/> 21	<input type="checkbox"/>
Page													<input type="checkbox"/>	<input type="checkbox"/>
Boundary Top					1982	2000	68.2					98.7	<input checked="" type="checkbox"/> 20	<input checked="" type="checkbox"/>
N 1		1972	2004	68.2	1982	2000	68.2		121			98.7	<input checked="" type="checkbox"/> 19	<input type="checkbox"/>
N 2		1970	1993	68.2	1974	1987	68.2		122.1			99.5	<input checked="" type="checkbox"/> 18	<input type="checkbox"/>
N 3		1959	1980	68.2	1965	1977	68.2		122.1			99.6	<input checked="" type="checkbox"/> 17	<input type="checkbox"/>
N 4		1949	1963	68.2	1958	1967	68.2		89.3			99.5	<input checked="" type="checkbox"/> 16	<input type="checkbox"/>
N 6		1929	1960	68.2	1944	1954	68.2		128			99.7	<input checked="" type="checkbox"/> 15	<input type="checkbox"/>
N 7		1945	1980	68.2	1938	1950	68.2		80.5			99	<input checked="" type="checkbox"/> 14	<input type="checkbox"/>
N 8		1945	1959	68.2	1935	1946	68.2		42.5			99.5	<input checked="" type="checkbox"/> 13	<input type="checkbox"/>
		Warning! Poor agreement - A= 42.5%(A/c= 60.0%)												
N 9		1917	1934	68.2	1922	1934	68.2		111.2			99.6	<input checked="" type="checkbox"/> 12	<input type="checkbox"/>
N 10		1900	1931	68.2	1907	1921	68.2		130.7			99.6	<input checked="" type="checkbox"/> 11	<input type="checkbox"/>
N 11		1904	1918	68.2	1897	1908	68.2		80			99.5	<input checked="" type="checkbox"/> 10	<input type="checkbox"/>
Top_Hat independent age		1885	1895	68.2									<input checked="" type="checkbox"/> 9	<input type="checkbox"/>
▲ Boundary Change		1885	1895	68.2	1891	1894	68.2		100			98.5	<input checked="" type="checkbox"/> 8	<input type="checkbox"/>
N 12		1885	1904	68.2	1886	1893	68.2		112.7			99.8	<input checked="" type="checkbox"/> 7	<input type="checkbox"/>
N 13		1869	1899	68.2	1874	1890	68.2		116.8			98.6	<input checked="" type="checkbox"/> 6	<input type="checkbox"/>
Boundary Lower					1866	1889	68.2					98.9	<input checked="" type="checkbox"/> 5	<input type="checkbox"/>
N 14		1489	1543	68.2	1492	1545	68.2		99.2			98.6	<input checked="" type="checkbox"/> 4	<input type="checkbox"/>
Boundary Bottom					1492	1545	68.2					98.6	<input checked="" type="checkbox"/> 3	<input type="checkbox"/>
▲ P_Sequence NeerlandsReid		-1.5	1.5	68.2	-1.515	-1.104	68.2		100			96.8	<input checked="" type="checkbox"/> 2	<input type="checkbox"/>

Figure 21: Table output of the Iterative model. All uncertainties are in 1-σ (68.2% certainty).

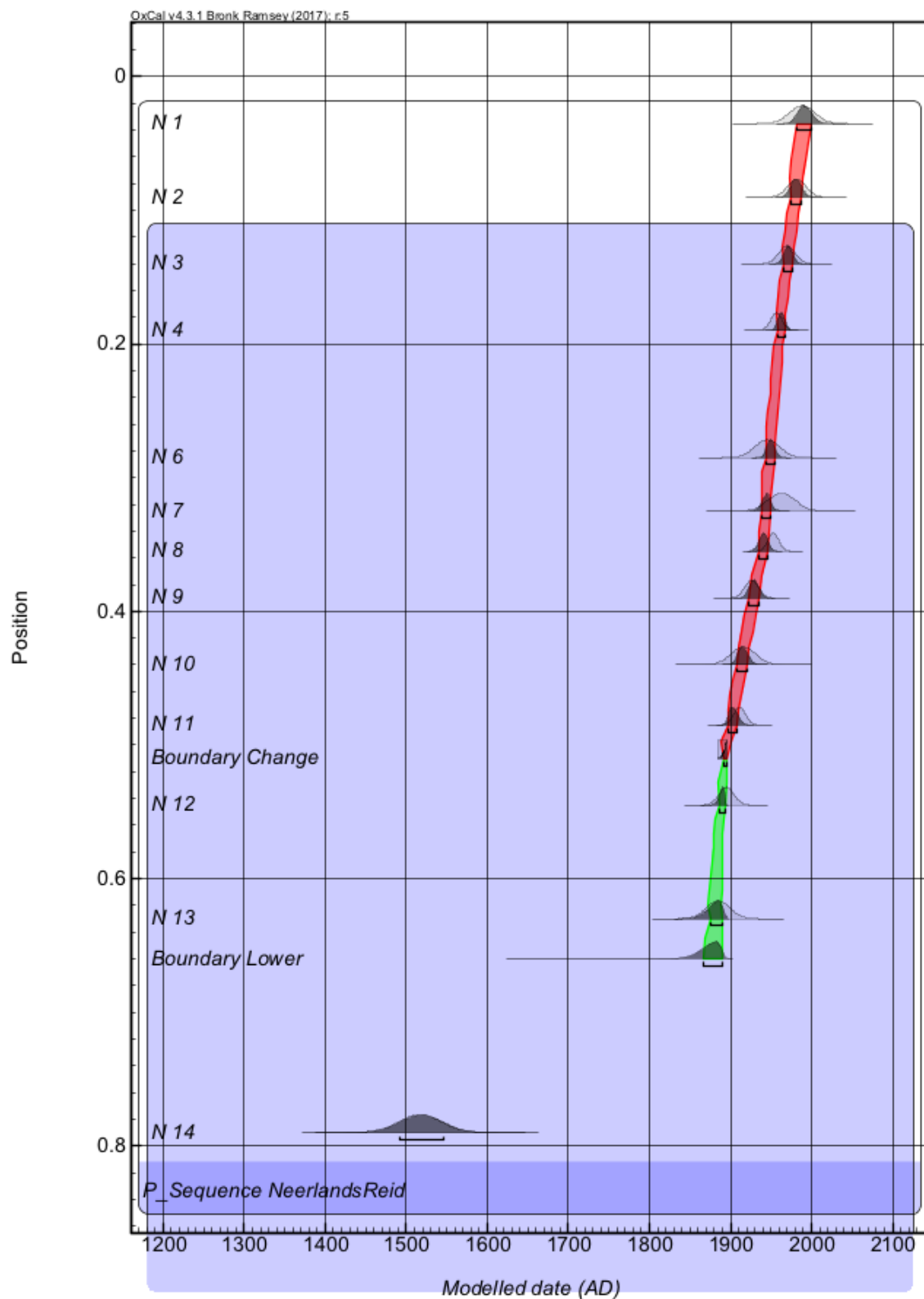


Figure 22: Age-depth model of the Iterative model. In red the salt marsh deposits and in green the underlying coastal plain deposits, separated by a boundary 'Boundary Change' with a top-hat-distribution at 51 cm depth. The position of 0 indicates the surface of the salt marsh at +1.51 NAP. For the sake of a better fit, a 'lower boundary' at 66 cm depth was added. Created using OxCal 4.3.1 (Bronk Ramsey, 2017)

5.10 Final age determination

As the OxCal model works without systematic error, these have to be re-added to come to a conclusive dating of the samples (Table 15).

Table 15: OxCal outcomes of the Iterative model, including re-added systematic errors for the samples

NR-#	Depth below surface (cm)	Age (AD)	Random error	Systematic error	Total error
1	3.5	1991	8.9	1.3	9.0
2	9.0	1981	6.8	1.5	7.0
3	14.0	1971	5.7	2.0	6.0
4	19.0	1963	4.6	2.6	5.3
6	28.5	1949	5.2	2.9	5.9
7	32.5	1944	5.8	2.1	6.1
8	35.5	1941	5.4	2.4	5.9
9	39.0	1929	5.9	3.4	6.8
10	44.0	1915	6.7	4.1	7.9
11	48.5	1903	5.4	5.5	7.8
12	54.5	1890	3.3	4.1	5.3
13	63.0	1883	8.0	4.4	9.1
14	79.0	1519	26.8	18.1	32.3

5.11 ^{137}Cs dates

When determining the DR-values from samples NR-11 to NR-14 and NR-A to NR-F, the gamma spectrometry of the results showed peaks in the ^{137}Cs spectrum of 661.65 keV in a number of the samples (Table 16). After combining the values with the measured depths, the sample at 19 cm depth shows the highest activity (Figure 23, Table 16). This depth is the same as OSL-sample NR-4, which is estimated to be from around 1963 ± 5 AD.

Table 16: ^{137}Cs activity in Bq/g per sample.

NR-#	^{137}Cs activity (Bq/g)	Uncertainty	Depth (cm)
A	9.04E-03	1.93E-04	12.0
B	4.74E-02	7.55E-04	19.0
C	2.24E-02	4.82E-04	24.0
D	1.06E-02	3.31E-04	31.0
E	2.18E-03	1.98E-04	36.0
F	7.38E-04	1.56E-04	41.0
11b	3.72E-04	9.20E-05	48.5
12	0		54.0
13	0		63.0
14	0		79.0

^{137}Cs Activity

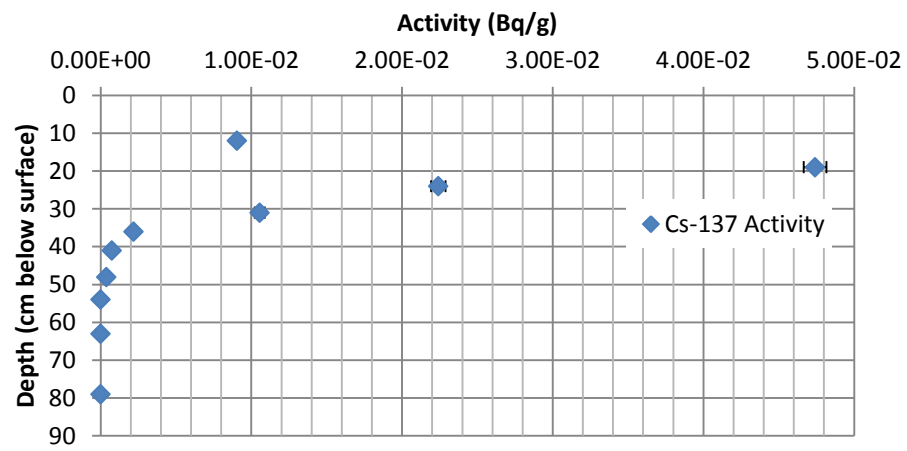


Figure 23: ^{137}Cs activity versus depth in cm below surface.

5.12 Accretion rates

A simple approach was used to reconstruct accretion rates. As depth and ages were known, accretion rates were simply calculated as the difference in sampling depth divided through the difference in determined age:

$$\text{accretion rate } \left(\frac{\text{cm}}{\text{year}} \right) = \frac{\text{difference in sampling depth (cm)}}{\text{difference in age (AD)}}$$

For consistency reasons with the rest of the reported data, the choice was made to work with the 1-sigma uncertainties. Sample NR-14 was not taken into account, as it stems from a different time period and it is unclear whether there has been continuous sedimentation since its deposition. Table 17 reports the outcomes and in Figure 24 the found accretion rates are visualised versus time. The large errors for the periods from 1941-1944 and 1944-1949 stem from the combination of a small difference in sampling depth (4.0 cm and 3.0 cm respectively), combined with a small difference in age between the sampling point (5.0 and 3.7 years respectively). For most of the periods, errors for the accretion rates are about as large as the determined values.

Table 17: Determined accretion speeds in between sampling points and associated ages of the depths for which the accretion speed was determined.

Difference in sampling depth	Difference in age (years)	Error (years)	Accretion speed (cm/year)	Error (cm/year)	Associated depth below surface (cm)	Associated age period (AD)	Error on age (years)
5.5	10.4	11.4	0.53	0.58	3.5-9.0	1981-1991	11.4
5.0	9.5	9.2	0.53	0.52	9.0-14.0	1971-1981	9.2
5.0	8.7	8.0	0.58	0.53	14.0-19.0	1963-1971	8.0
9.5	13.3	8.0	0.71	0.43	19.0-28.5	1949-1963	8.0
4.0	5.0	8.5	0.80	1.38	28.5-32.5	1944-1949	8.5
3.0	3.7	8.5	0.82	1.88	32.5-35.5	1941-1944	8.5
3.5	11.9	9.0	0.29	0.22	35.5-39.0	1929-1941	9.0
5.0	14.1	10.4	0.35	0.26	39.0-44.0	1915-1929	10.4
4.5	11.6	11.1	0.39	0.37	44.0-48.5	1903-1915	11.1
6.0	13.2	9.4	0.45	0.32	48.5-54.5	1890-1903	9.4
8.5	7.0	10.5	1.22	1.84	54.5-63.0	1883-1890	10.5

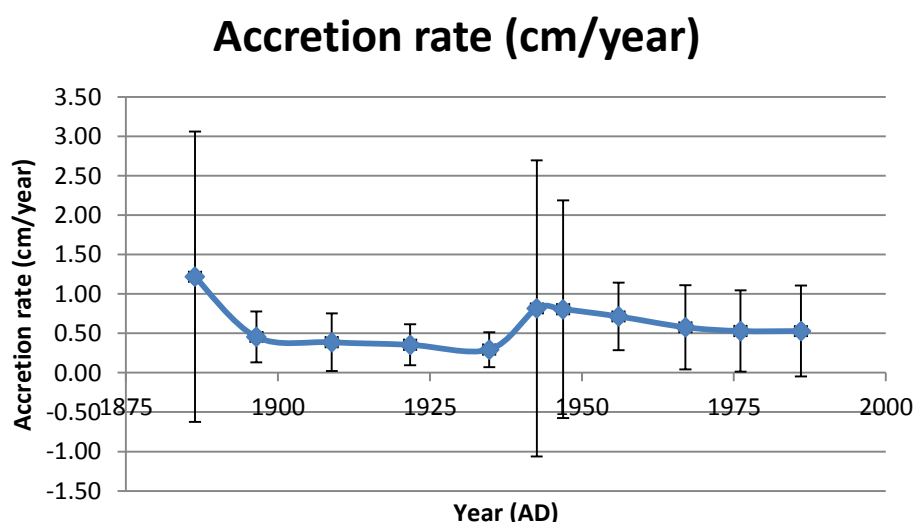


Figure 24: Accretion rate in cm/y through time

6. Discussion

The goal of this research was to reconstruct accretion rates on the Neerlands Reid salt marsh at Ameland. A secondary goal of the research was to see whether a change in accretion rates had occurred since 1986, when the exploitation of an underlying gas field commenced, leading to a cup-shaped subsidence basin in the area (Figure 2, Krol, 2014). As accretion rates have been physically measured on multiple locations on the salt marsh for the period of 1988 to 2014 by Krol (2014)(Figure 4), it is possible to make a comparison between reconstructed historic and recent accretion rates.

Overall, the chosen protocols (SAR, Iterative model, OxCal) seem to have produced reliable dating of the samples, as the results show a good fit with the independent age control of 1890 at 51 cm depth and are in a logical chronographic order. Sample NR-5 was treated as an outlier and removed from further analysis, due to the shape of its D_e -distribution (Figure 15e), its probability density function (Figure 17e) and its bleaching indicators (Table 9).

Samples NR-1 to NR-4, as well as NR-10 score higher on bleaching indicators than the rest of the samples (Table 9). This can potentially have led to an overestimation of the ages for these samples, as poorly bleached grains have been used in the analysis (Wallinga, 2002b). There are some indications of bioturbation for samples NR-7 to NR-10 and NR-13, as these showed negative skewness factors (Table 9),(Madsen et al., 2011).

The choice was made to use the Iterative model for the analysis of the D_e -distributions, as it gave the overall best results when taking the whole profile into account. If only the samples NR-1 to NR-4 would have been analysed, one might have opted for the bootstrapped likelihood MAM3_{ul}, due to the higher poor-bleaching indicators for these samples. However, this was not fitting for the rest of the data, as the negative skewness of samples NR-7 to NR-10 would have potentially lead to an underestimation of the ages. As using different models for different parts of the profile was not desirable, the choice was made to stick with the Iterative model, which overall also gave the best fit for the OxCal model (Bronk Ramsey, 1995, Bronk Ramsey, 2008).

Another choice that was made is to not include an error on depth. The assumption was made that the D_e -distribution of each sample is build up out of grains equally spread from any depth within the sampling tube and that depth differences for separate luminescent grains would average out towards the centre of the used tube. For the bootstrapped likelihood MAM3_{ul}; D_e -distributions a small correction on the sampling depth was taken into account, as the procedure is selecting the aliquots with the lowest D_e -values which are more likely to be from the top half of the sampling tube.

The reconstructed accretion rates in this research seem rather stable since the mid-sixties at a rate around 0.58 ± 0.53 cm/year, with a slight decrease towards 0.53 ± 0.58 cm/year since approximately 1971 (Table 17, Figure 24). For the period between 1941 and 1949, much higher accretion rates are reported of 0.80 cm/year and 0.82 cm/year, but the errors on these reconstructed accretion rates are so large (1.34 cm/year and 1.81 cm/year respectively, Table 17), that it is hard to determine any form of trend.

The reconstructed accretion rates can be compared to rates found in a yearly monitoring series done from 1988 to 2014 on a number of buried tiles on the same salt marsh by Krol (2014). Krol reports accretion rates ranging from 0.0 to 0.8 cm/year were found. If we look closer at these measurements, four are on a locations which are comparable to the location sampled in this research (Figure 5). At point T01 (Figure 4), on a levee position alike the one sampled here, an accretion rate of 0.8 cm/year was measured. Also point T04 and T07 are comparable as they are both mainly supplied by water and sediment through the Oerdsloot, the same creek of which the levee was sampled in this research. These two points show accretion rates of 0.5 and 0.6 cm/year, which is seen as 'normal' for this salt marsh (Krol, 2014). Point T17 is an outlier, as the vegetation at this location has been squashed by livestock leading to a bare spot where water accumulates and some erosion occurs, leading to a negative accretion rate.

As the sampling position in this research (white arrow in Figure 4) was further inland than the morphologically best comparable location (T01), the lower accretion rate can be explained due to the larger distance to the Wadden Sea, as sediment accumulation tends to decrease with distance to the seaward edge of the salt marsh (Reed, 1988). Accretion rates on measuring locations T04 and T07 show the best match with the rates found in this research. This is likely because although they are located

much closer to the seaward edge of the salt marsh, the distance to the creek is larger, lowering accretion rates (French and Spencer, 1993; Chmura and Hung, 2004). Overall, the reconstructed accretion rates for the upper part of the profile are very comparable to those found in the field. Despite the subsidence in the subsoil, the hypothesised increase of accretion rates was not found, which can have a number of causes.

It has been shown that the closing of the Zuiderzee, the current IJsselmeer, in 1932 increased tidal amplitudes throughout the Wadden Sea, especially close to the former inlets, though the changes were very limited in the area around Ameland (Doekes, 1985). The closing of the Zuiderzee also led to an increased hunger for sediments within the Wadden Sea basin. It is predicted that the still ongoing process of adjustment to new situation will continue for approximately another century (Vroom et al., 2014).

It is likely that the more recent closing of the nearby Lauwerszee in 1969 has had a much larger effect on the Neerlands Reid salt marsh at Ameland due to its much closer proximity. Wang (2007) reports a slight decrease of tidal amplitude and an increase of accommodation space within the local tidal basin in the area around Ameland, Schiermonnikoog, which lies more to the east, and a sandbank named the Engelsmanplaat in between due to the closing of the Lauwerszee. This led to a deficit of sediments in the Wadden Sea side of the estuary, potentially hampering the accretion speed on the salt marsh. In the same paper it is mentioned that another effect of this process is a surplus of sediment on the North Sea side outer delta of the estuary, though this is contradicted by Vroom et al. (2014) and the ongoing process of anthropogenic sand suppletions on the North Sea coast of Ameland since 1980 (Dankers et al., 1983) also seems to contradict this statement. This deficit of sediments in the Wadden Sea side of the estuary could very well be a reason that the Neerlands Reid seems to not have responded to the subsidence in the deep subsoil.

There is potential for ^{137}Cs -dating in this kind of research, especially to determine the accretion rate of the last decades. It would however then be necessary to sample at a much higher resolution than was done in this research. It seems reasonable to assume that the clear visible ^{137}Cs activity peak is the result of the Chernobyl accident in 1986 (Walker, 2005; Madsen et al., 2005). However, as sampling resolution is low, it is unclear where the true peak is located between the upper and underlying sampling points and whether there is mixing with ^{137}Cs from the Sellafield nuclear complex from around 1980 (Madsen et al., 2005). Therefore we can only state that the expected 1986-peak is at somewhere between 12 and 24 centimetres depth, which does not contradict the 1-sigma OxCal dating results as this is between NR-2 (9 cm depth, 1981 ± 7.0) and NR-6 (28.5 cm depth, 1949 ± 5.9). In a comparison research of OSL, ^{210}Pb and ^{137}Cs on a tidal mud flat in Ho Bugt, Denmark by Madsen et al. (2005) maximum activity values of around $5.0 \cdot 10^{-2}$ Bq/g were found, with ^{137}Cs -activity above $4.0 \cdot 10^{-2}$ Bq/g over a 10 cm range below the peak. This is comparable to the highest found ^{137}Cs activity in sample NR-B of $0.47 \cdot 10^{-2}$ Bq/g at 19 cm depth.

There are indications of illuviation of ^{137}Cs within the profile, as traces of ^{137}Cs are found down to a depth of 48 cm. This depth is just above the deepest salt marsh deposits, which according to multiple sources and historical maps developed no later than the beginning of the 20th century, decades before the first emissions of ^{137}Cs . Another problem is the diameter of the used sampling tubes of 4.5 cm, adding a 2.25 cm error on the sampling depth for the ^{137}Cs dating. The choice was made to not incorporate this depth error in the OSL-dating, as this is built up out of multiple luminescent grains from throughout the tube and the expectation is that this averages out towards the mentioned depth. For the higher depth resolution needed for ^{137}Cs dating this does form a very important source of uncertainty.

7. Conclusion

The goals of this research were achieved. Using a combination of OSL dating and Bayesian statistics, it was possible to reconstruct accretion rates at the salt marsh Neerlands Reid at Ameland. Values in the order of 0.5 ± 0.5 cm/year were found, these rate are in close agreement with physically measured accretion rates on the same salt marsh. A hypothesised increase of the accretion rate since the last thirty years due to subsidence underneath the area caused by gas-extraction in the area was not found, as the results showed a stable accretion rate for the last 50 years. We hypothesise that this lack of reaction could possibly be explained as a result of the ongoing adjustment of the estuary to closing of the Lauwerszee in 1969, which has lead to an increased accommodation space in the estuary causing a lower sediment supply for the salt marsh. However, this would be an hypothesis for a new research project.

8. Recommendations

In this research, an attempt was made to reconstruct accretion rates for the last 130 years on a salt marsh at Ameland. It turned out to be possible to accurately reconstruct accretion rates, however, the precision is rather low, as the lowest uncertainties found are still about as large as the found values. It is therefore hard to make statements, especially on short-term trends.

There were no indications of the hypothesised increase of accretion rates in the last thirty years. We hypothesise that this could have something to do with the ongoing adaptation of the estuary to the closing of the Lauwerszee in 1969. However, more research is needed in order to make any valid statements on this.

9. Acknowledgements

This work was supported by the Strategic Knowledge Program of the Dutch Ministry of Economic Affairs (KB-24-002-005). We are grateful to the commons of Neerlands Reid for permission to undertake our investigation on their property.

I really enjoyed writing this thesis and at the end of it, I would like to sincerely thank everyone I have worked with for their support in the recent period. Not only on an academic level, but especially on a personal level. In the period I wrote this thesis I went through a rough time in my personal life and the support and understanding of the staff was heart warming and pulled me through when I needed it most.

Thank you Jakob, Tony, Pieter and Loek for your support and feedback on the delivered work.

Thank you Alice and Erna for helping me out in the lab, the first days in the subdued light were quite rough, but when my lab-time was over I really missed working there.

And special thanks to my girlfriend Emma, not only for the support and being an independent sparring partner, but most of all because without you I would never have been able to get myself out of bed in the mornings to start working on my thesis.

References

- Aitken, M. J. (1985). *Thermoluminescence Dating*. Academic Press.
- Aitken, M. J. (1998). *Introduction to optical dating: the dating of Quaternary sediments by the use of photon-stimulated luminescence*. Clarendon Press.
- Arnold, L. J., Roberts, R. G., Galbraith, R. F., & DeLong, S. B. (2009). A revised burial dose estimation procedure for optical dating of young and modern-age sediments. *Quaternary Geochronology*, 4(4), 306-325.
- Audet, D. M. (1995). Mathematical modelling of gravitational compaction and clay dehydration in thick sediment layers. *Geophysical Journal International*, 122(1), 283-298.
- Bailey, R. M., & Arnold, L. J. (2006). Statistical modelling of single grain quartz De distributions and an assessment of procedures for estimating burial dose. *Quaternary Science Reviews*, 25(19), 2475-2502.
- Ballarini, M., Wallinga, J., Murray, A. S., Van Heteren, S., Oost, A. P., Bos, A. J. J., & Van Eijk, C. W. E. (2003). Optical dating of young coastal dunes on a decadal time scale. *Quaternary Science Reviews*, 22(10), 1011-1017.
- Bartholdy, J., Christiansen, C., & Kunzendorf, H. (2004). Long term variations in backbarrier salt marsh deposition on the Skallingen peninsula—the Danish Wadden Sea. *Marine Geology*, 203(1), 1-21.
- Bronk Ramsey, C. (1995). Radiocarbon calibration and analysis of stratigraphy: the OxCal program. *Radiocarbon*, 37(02), 425-430.
- Bronk Ramsey, C. (2008). Deposition models for chronological records. *Quaternary Science Reviews*, 27(1), 42-60.
- Bronk Ramsey, C. (2017). OxCal 4.3.1 *Web Interface Build (78)*.
- Chmura, G. L., & Hung, G. A. (2004). Controls on salt marsh accretion: A test in salt marshes of Eastern Canada. *Estuaries*, 27(1), 70-81.
- Cunningham, A. C., & Wallinga, J. (2010). Selection of integration time intervals for quartz OSL decay curves. *Quaternary Geochronology*, 5(6), 657-666.
- Cunningham, A. C., & Wallinga, J. (2012). Realizing the potential of fluvial archives using robust OSL chronologies. *Quaternary Geochronology*, 12, 98-106.
- Cunningham, A. C., Wallinga, J., Hobo, N., Versendaal, A. J., Makaske, B., & Middelkoop, H. (2015). Re-evaluating luminescence burial doses and bleaching of fluvial deposits using Bayesian computational statistics. *Earth Surface Dynamics*, 3(1), 55.
- Dankers, N., Binsbergen, M., Zegers, K. (1983). De effecten van zandsuppletie op de fauna van het strand van Texel en Ameland. Rijksinstituut voor Natuurbeheer, Texel. 14 p.
- Davidson-Arnott, R. G., van Proosdij, D., Ollerhead, J., & Schostak, L. (2002). Hydrodynamics and sedimentation in salt marshes: examples from a macrotidal marsh, Bay of Fundy. *Geomorphology*, 48(1), 209-231.
- Doekes, J., (1985). De invloed van de afsluiting van de Zuiderzee op het getij in de Waddenzee. *Rijkswaterstaat, RIKZ (Dienst Getijdewateren)*. 41 pp.
- Duller, G. A. T. (2003). Distinguishing quartz and feldspar in single grain luminescence measurements. *Radiation measurements*, 37(2), 161-165.
- Dunne, T., & Leopold, L. B. (1978). *Water in environmental planning*. Macmillan.
- Ezer, T., Haigh, I. D., & Woodworth, P. L. (2015). Nonlinear sea-level trends and long-term variability on western European coasts. *Journal of Coastal Research*, 32(4), 744-755.

- French, J. (2006). Tidal marsh sedimentation and resilience to environmental change: exploratory modelling of tidal, sea-level and sediment supply forcing in predominantly allochthonous systems. *Marine Geology*, 235(1), 119-136.
- French, J. R., & Spencer, T. (1993). Dynamics of sedimentation in a tide-dominated backbarrier salt marsh, Norfolk, UK. *Marine Geology*, 110(3-4), 315-331.
- French, J. R., & Stoddart, D. R. (1992). Hydrodynamics of salt marsh creek systems: Implications for marsh morphological development and material exchange. *Earth surface processes and landforms*, 17(3), 235-252.
- Friedrichs, C. T., & Perry, J. E. (2001). Tidal salt marsh morphodynamics: a synthesis. *Journal of Coastal Research*, special issue 27, 7-37.
- Galbraith, R. F., Roberts, R. G., Laslett, G. M., Yoshida, H., & Olley, J. M. (1999). Optical dating of single and multiple grains of quartz from Jinmium rock shelter, northern Australia: Part I, experimental design and statistical models. *Archaeometry*, 41(2), 339-364.
- Guérin, G., Mercier, N., & Adamiec, G. (2011). Dose-rate conversion factors: update. *Ancient TL*, 29(1), 5-8.
- Guilcher, A. (1969). Pleistocene and Holocene sea level changes. *Earth-Science Reviews*, 5(2), 69-97.
- Hobo, N., Makaske, B., Middelkoop, H., & Wallinga, J. (2010). Reconstruction of floodplain sedimentation rates: a combination of methods to optimize estimates. *Earth Surface Processes and Landforms*, 35(13), 1499-1515.
- Huntley, D. J., Godfrey-Smith, D. I., & Thewalt, M. L. (1985). Optical dating of sediments. *Nature*, 313(5998), 105-107.
- Hütt, G., & Jaek, I. (1989). Infrared stimulated photoluminescence dating of sediments. *Ancient TL*, 7(3), 48-51.
- IPCC (2013): *Climate Change 2013: The Physical Science Basis. Contribution of Working Group I contribution to the Fifth Assessment Report of the Intergovernmental Panel on Climate Change* [Stocker, T.F., D. Qin, G.-K. Plattner, M. Tignor, S.K. Allen, J. Boschung, A. Nauels, Y. Xia, V. Bex and P.M. Midgley (eds.)]. Cambridge University Press, Cambridge, United Kingdom and New York, NY, USA, 1535 pp.
- ISRIC (2016): Vlakvaaggrond Ameland, 'Kwelder als buffer bij zeespiegelstijging' Neerlands Reid in wording: Stephan Mantel, Pieter Slim & Johan Krol.
<http://library.wur.nl/WebQuery/wurpubs/fulltext/366733>
- Ketelaar, G., van der Veen, W. & Doornhof, D. (2011). Monitoring effecten van bodemdaling op Ameland-Oost, 1. Bodemdaling, in: de Vlas, J. (Ed.), Monitoring effecten van bodemdaling op Ameland-Oost; evaluatie na 23 jaar gaswinning. Begeleidingscommissie Monitoring Bodemdaling Ameland, [Assen], pp. 9-28.
- King, S. E., & Lester, J. N. (1995). The value of salt marsh as a sea defence. *Marine pollution bulletin*, 30(3), 180-189.
- Kirwan, M. L., Temmerman, S., Skeeahan, E. E., Guntenspergen, G. R., & Fagherazzi, S. (2016). Overestimation of marsh vulnerability to sea level rise. *Nature Climate Change*, 6(3), 253-260.
- KNMI (2015): KNMI'14-klimaatscenario's voor Nederland; Leidraad voor professionals in klimaatadaptatie, KNMI, De Bilt, 34 pp.
- Krol, J. (2014). Korte rapportage opslibbingsmetingen met ondergrondse tegels, Natuurcentrum Ameland, Nes Ameland, 8 pp.
- Lamb, P. J., & Pepler, R. A. (1987). North Atlantic Oscillation: concept and an application. *Bulletin of the American Meteorological Society*, 68(10), 1218-1225.

- Madsen, A. T., & Murray, A. S. (2009). Optically stimulated luminescence dating of young sediments: a review. *Geomorphology*, 109(1), 3-16.
- Madsen, A. T., Murray, A. S., Andersen, T. J., Pejrup, M., & Breuning-Madsen, H. (2005). Optically stimulated luminescence dating of young estuarine sediments: a comparison with ²¹⁰Pb and ¹³⁷Cs dating. *Marine Geology*, 214(1), 251-268.
- Madsen, A. T., Murray, A. S., Jain, M., Andersen, T. J., & Pejrup, M. (2011). A new method for measuring bioturbation rates in sandy tidal flat sediments based on luminescence dating. *Estuarine, Coastal and Shelf Science*, 92(3), 464-471.
- Mejdahl, V. (1979). Thermoluminescence dating: Beta-dose attenuation in quartz grains. *Archaeometry*, 21(1), 61-72.
- Murray, A. S., & Wintle, A. G. (2000). Luminescence dating of quartz using an improved single-aliquot regenerative-dose protocol. *Radiation Measurements*, 32(1), 57-73.
- Murray, A. S., & Wintle, A. G. (2003). The single aliquot regenerative dose protocol: potential for improvements in reliability. *Radiation measurements*, 37(4), 377-381.
- Olley, J. M., Pietsch, T., & Roberts, R. G. (2004). Optical dating of Holocene sediments from a variety of geomorphic settings using single grains of quartz. *Geomorphology*, 60(3), 337-358.
- Prescott, J. R., & Hutton, J. T. (1994). Cosmic ray contributions to dose rates for luminescence and ESR dating: large depths and long-term time variations. *Radiation measurements*, 23(2), 497-500.
- Preusser, F., Degering, D., Fuchs, M., Hilgers, A., Kadereit, A., Klasen, N., Krbetschek, M., Richter, D. & Spencer, J. Q. (2008). Luminescence dating: basics, methods and applications. *Quaternary Science Journal*, 57(1-2), 95-149.
- Provinciaal Overlegorgaan Kust (2000) Dynamisch kustbeheer : kustzone midden en oost Ameland : een advies over het beheer van de zandige kustzone op Ameland van km 7 tot km 23 *Provinciaal Overlegorgaan Kust Fryslân, Projectgroep midden en oost Ameland*. 23 pp.
- Redfield, A. C. (1972). Development of a New England salt marsh. *Ecological monographs*, 42(2), 201-237.
- Reed, D. J. (1988). Sediment dynamics and deposition in a retreating coastal salt marsh. *Estuarine, Coastal and Shelf Science*, 26(1), 67-79.
- Reed, D. J. (1990). The impact of sea-level rise on coastal salt marshes. *Progress in Physical Geography*, 14(4), 465-481.
- Rhodes, E. J., Ramsey, C. B., Outram, Z., Batt, C., Willis, L., Dockrill, S., & Bond, J. (2003). Bayesian methods applied to the interpretation of multiple OSL dates: high precision sediment ages from Old Scatness Broch excavations, Shetland Isles. *Quaternary Science Reviews*, 22(10), 1231-1244.
- Rijkswaterstaat (2016): http://getij.rws.nl/getij_resultaat.cfm?page=home&from=2016-08-26&from2=03-11-2016&location=NES&Timezone=MET_DST&refPlane=NAP 03/11/2016 11:14
- Schuerch, M., Rapaglia, J., Liebetrau, V., Vafeidis, A., & Reise, K. (2012). Salt marsh accretion and storm tide variation: an example from a barrier island in the North Sea. *Estuaries and Coasts*, 35(2), 486-500.
- Slim, P.A., Wegman, R.M.A., Sanders, M.E., Huiskes, H.P.J., van Dobben, H.F. (2011). 2.7 Monitoring kwelderrand Oerderduinen; Onderzoek naar de effecten van bodemdaling door gaswinning op de morfologie en vegetatie van de kuststrook ten zuiden van Het Oerd en de Oerderduinen op Oost-Ameland: 125-176. In: Monitoring effecten van bodemdaling op Ameland-Oost; evaluatie na 23 jaar gaswinning. Deel 1. Begeleidingscommissie Monitoring Bodemdaling Ameland, [Assen].

- Temmerman, S., Govers, G., Wartel, S., & Meire, P. (2004). Modelling estuarine variations in tidal marsh sedimentation: response to changing sea level and suspended sediment concentrations. *Marine Geology*, 212(1), 1-19.
- Townend, I., Fletcher, C., Knappen, M., & Rossington, K. (2011). A review of salt marsh dynamics. *Water and Environment Journal*, 25(4), 477-488.
- Uncles, R. J., Stephens, J. A., & Smith, R. E. (2002). The dependence of estuarine turbidity on tidal intrusion length, tidal range and residence time. *Continental Shelf Research*, 22(11), 1835-1856.
- USGS, 1997. Global Warming, Sea-level Rise, and Coastal Marsh Survival. United States Geological Survey. FS-091-97, 2 pp.
- Vandenbergh, D., De Corte, F., Buylaert, J. P., & Kučera, J. (2008). On the internal radioactivity in quartz. *Radiation Measurements*, 43(2), 771-775.
- Vlas, J. de, (2005). Monitoring effecten van bodemdaling op Ameland-Oost; Evaluatie na 18 jaar gaswinning. Begeleidingscommissie Monitoring Bodemdaling Ameland, Assen.
- Vroom, J., Wang, B., Valk, B. van der, Oost, A. (2014). Sedimentaire systeem van de Waddenzee. Deltares, Delft.
- Waddenzee.nl Retrieved from <http://www.waddenzee.nl/themas/bodemdaling-ameland/> 13/03/2017 14:35
- Wahlgren, M. A., & Nelson, D. M. (1972). Radiological and Environmental Research Division Annual Report, Part III: Ecology. *Argonne National Laboratory ANL-7960*, 7-14.
- Wallinga, J. (2002a). Optically stimulated luminescence dating of fluvial deposits: a review. *Boreas*, 31(4), 303-322.
- Wallinga, J. (2002b). On the detection of OSL age overestimation using single-aliquot techniques. *Geochronometria*, 21(1), 17-26.
- Walker, M. J. C. (2005). *Quaternary dating methods*. John Wiley and Sons.
- Wang, Z. B. (2007). Morfologische ontwikkeling van het Rif en de Engelsmanplaat. Analyse naar mogelijke invloed van de bodemdaling. Commissie Monitoring Bodemdaling Ameland, Assen. 56 pp.
- Wintle, A. G. (1997). Luminescence dating: laboratory procedures and protocols. *Radiation Measurements*, 27(5), 769-817.
- Wintle, A. G., & Murray, A. S. (2006). A review of quartz optically stimulated luminescence characteristics and their relevance in single-aliquot regeneration dating protocols. *Radiation Measurements*, 41(4), 369-391.

Appendix A: Sieving results

NR-#	Work sample weight (g)	<180 (g)	180-212 (g)	212-250 (g)	>250 (g)	<180 (%)	180-212 (%)	212-250 (%)	>250 (%)
1	27.1	19	2.1	0.6	0.3	70.1	7.7	2.2	1.1
2	38.9	23.9	1.3	0.1	2.6	61.4	3.3	0.3	6.7
3	44.3	26.7	2	0.8	1.7	60.3	4.5	1.8	3.8
4	46.2	27	2.1	0.2	1.4	58.4	4.5	0.4	3.0
5	appr. 45	24.2	4.4	1.3	1	53.8	9.8	2.9	2.2
6	44.6	27.7	3	0.7	1.1	62.1	6.7	1.6	2.5
7	46.4	26	6	2.1	0.9	56.0	12.9	4.5	1.9
8	47.5	24.1	8.3	2.7	1.7	50.7	17.5	5.7	3.6
9	48.7	27.2	9.5	0.2	0.5	55.9	19.5	0.4	1.0
10	48.9	30.9	3.4	0.6	0.4	63.2	7.0	1.2	0.8
NR-#	Work sample weight (g)	<180 (g)	180-212 (g)	>212 (g)		<180 (%)	180-212 (%)	>212 (%)	
11	199.9	104.06	9.7	3.18		52.1	4.9	1.6	
12	227.4	133.24	58.97	8.51		58.6	25.9	3.7	
13	199.9	112.59	52.6	15.33		56.3	26.3	7.7	
14	231.2	124.01	24.12	18.73		53.6	10.4	8.1	

Appendix B: Porosity and Field capacity per texture class

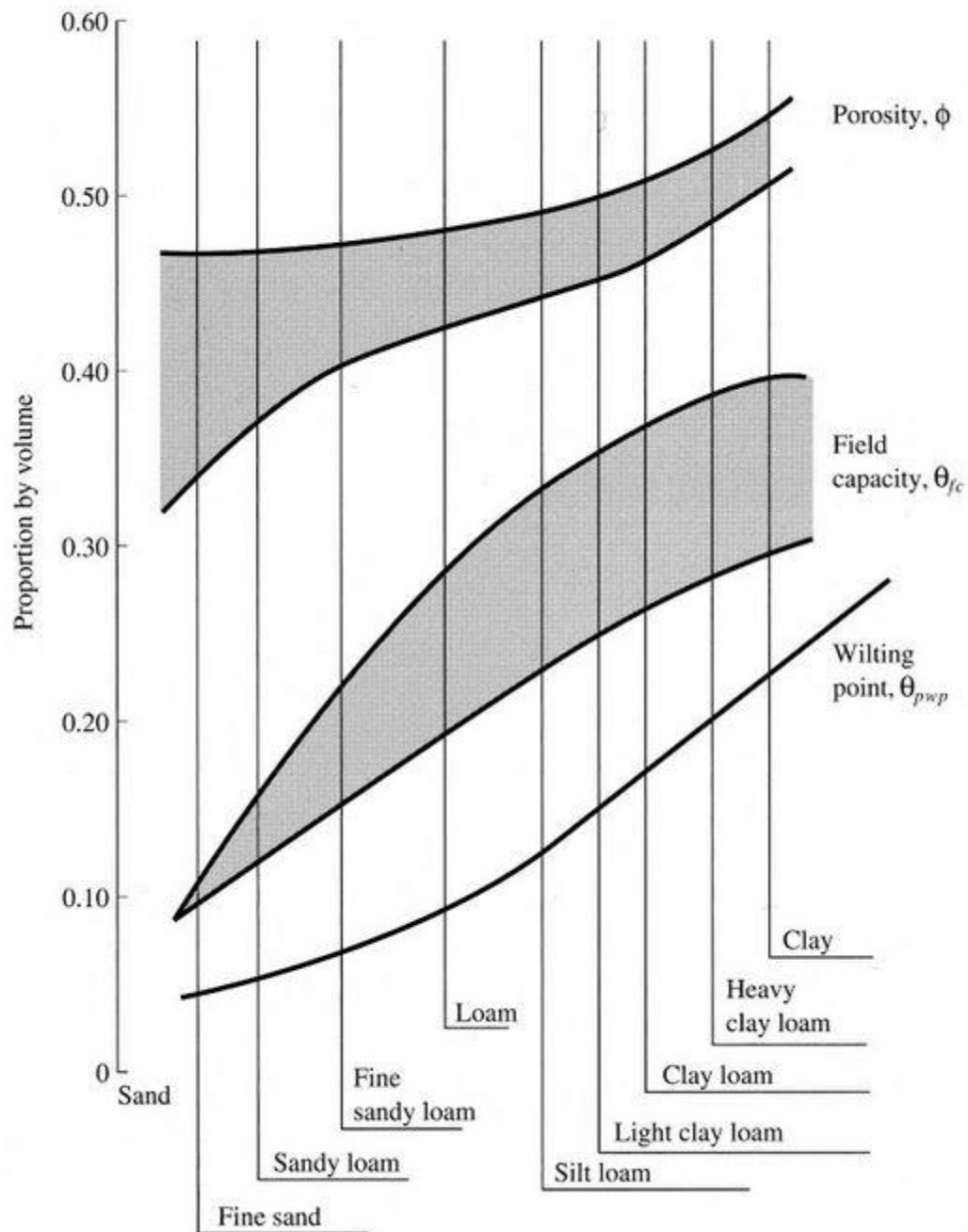


Figure 25: Porosity and Field capacity for multiple texture classes (from Dunne and Leopold, 1978).

Appendix C: Used formulas for calculations

$$\text{Shallowness correction} = 0.5 + 0.1141 \left(1 - 2.7128^{-0.0407 * \text{depth}(m) * 100 * \frac{\rho}{1.3}} \right) + 0.3844 \left(1 - 2.7128^{-0.0763 * \text{depth}(m) * 100 * \frac{\rho}{1.3}} \right)$$

After Madsen et al. (2005), corrected by J Wallinga (2013)

Appendix D: Oxcal script

Plot()

```
{P_Sequence("NeerlandsReid",1000,50, U(-1.5,1.5))

{Boundary("Bottom") {}};

Date("14",N(1516.8,26.5))    { z=0.79; };

Boundary("Lower")           { z=0.66; };

Date("13",N(1884.7,14.7))    { z=0.63; };

Date("12",N(1895.0,9.3))     { z=0.545; };

Boundary("Change", Top_Hat("independent age",1890,5)) {z=0.51; };

Date("11",N(1911.4,7.2))     { z=0.485; };

Date("10",N(1915.9,15.3))    { z=0.44; };

Date("9",N(1926.1,8.4))      { z=0.39; };

Date("8",N(1952.8,6.7))      { z=0.355; };

Date("7",N(1963,16.7))       { z=0.325; };

Date("6",N(1945.2,15.4))     { z=0.285; };

Date("4",N(1956.7,7.1))      { z=0.19; };

Date("3",N(1969.7,10.1))     { z=0.14; };

Date("2",N(1981.8,11.3))     { z=0.09; };

Date("1",N(1988.5,15.7))     { z=0.035; };

Boundary("Top")             {};

};

};
```

Appendix E: Map of the research area in 1854



Figure 26: Snip of the map of Ameland in 1854. White arrow indicating approximate sampling location. Original map from Tresoar: <http://www.frieskaartenkabinet.nl/en/fries-kaartenkabinet/04992>

Appendix F: Map of the research area in 1888

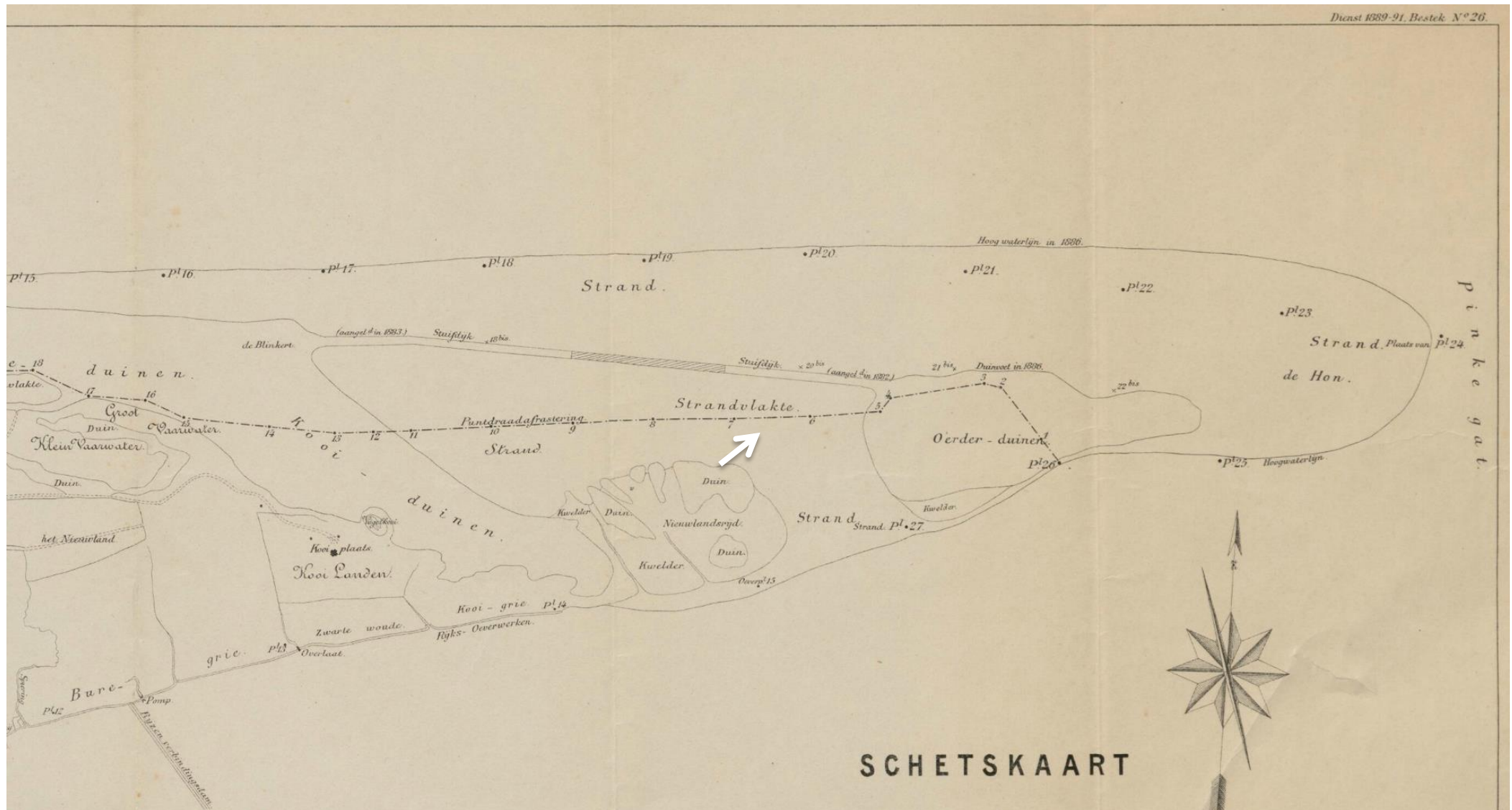


Figure 27: Snip of the map of Ameland in 1888. White arrow indicating approximate sampling location. Original map from Tresoor: <http://www.frieskaartenkabinet.nl/en/fries-kaartenkabinet/04321>

Appendix G: Map of the research area in 1897, created in 1910



Figure 28: Snip of the map of Ameland in 1897, produced in 1910. White arrow indicating approximate sampling location. Original map from Treasoar: <http://www.frieskaartenkabinet.nl/en/fries-kaartenkabinet/04376>